

Extreme mass ratio inspirals in galaxies with dark matter halos

Ning Dai (戴宁) ^{1,*} Yungui Gong (龚云贵) ^{2,1,†} Yang Zhao (赵阳) ^{1,‡} and Tong Jiang (江通) ^{3,§}

¹*School of Physics, Huazhong University of Science and Technology, Wuhan, Hubei 430074, China*

²*Institute of Fundamental Physics and Quantum Technology,
Department of Physics, School of Physical Science and Technology,
Ningbo University, Ningbo, Zhejiang 315211, China*

³*College of Physics and Technology, Kunming University, Kunming 650214, China*

Using an analytic, static, and spherically symmetric metric for a Schwarzschild black hole immersed in a dark matter (DM) halo with the Hernquist-type profile, we derive analytic expressions for the orbital period and precession of eccentric extreme mass ratio inspirals (EMRIs) surrounded by DM halos, and we show how the precession rates decrease and even undergo a prograde-to-retrograde precession transition if the density of DM halo is large enough. The presence of local DM halos also retards the decrease of the semi-latus rectum and the eccentricity. The orbital evolution of EMRIs immersed in DM halos is then calculated numerically by considering the combined effects of gravitational radiation reaction, dynamical friction, and accretion. Comparing the number of orbital cycles accumulated over a one-year evolution for EMRIs with and without DM halos, we find that DM halos with compactness as small as 10^{-5} can be detected. From the mismatch between gravitational waveforms of EMRIs with and without DM halos, we show that EMRIs in galaxies can be used to probe the existence of DM halos and detect the compactness of DM halos as small as 10^{-5} . Employing the Fisher information matrix method, we find that larger compactness and density values of DM halos help to reduce the estimation error of parameters and further break the degeneracy between the parameters.

I. INTRODUCTION

The first detection of gravitational wave (GW) from the merger of a black hole (BH) binary by the LIGO Scientific Collaboration and the Virgo Collaboration in 2015 [1, 2] opened a new window for probing gravitational physics and fundamental physics. Since then, tens of confirmed GW events have been detected by the ground-based GW observatories [3–6]. The ground-based GW observatories are only sensitive to GWs in the frequency range of $10 - 10^3$ Hz. The space-based GW observatories such as LISA [7–9], TianQin [10], and Taiji [11, 12] will usher a new era in GW astronomy due to their unprecedented accuracy and their sensitive band of mHz [13–16]. One particularly interesting target of space-based GW detectors is the case of a stellar-mass compact object (SCO) inspiraling into a massive black hole (MBH)-the extreme mass ratio inspirals (EMRIs) [17]. There are $10^5 - 10^6$ GW cycles in the detector band when the SCO inspirals deep inside the strong field region of the MBH, and rich information about the spacetime geometry around the MBH is encoded in the GW waveform. Therefore, the observations of GWs emitted from EMRIs present us a pristine opportunity for the study of astrophysics, gravity in the strong and nonlinear regions, and the nature of BHs [18–22].

Although the property of dark matter (DM) is still a mystery in particle physics, there is a plethora of indirect

evidence for the existence of DM in the Universe [23–32]. DM may cluster at the centers of galaxies and around BHs [33–36], and affect the dynamics of binaries, and hence the GWs emitted from them. Since EMRIs are believed to reside in stellar clusters and the centers of galaxies, DM may affect the dynamics of EMRIs and be detectable in the observations of GWs from EMRIs. In particular, those EMRIs immersed in DM environment may be used to understand the astrophysical environment surrounding them, probably confirm the existence of DM and uncover the nature of DM [37–52].

In the studies of DM effects, Newtonian approaches were usually applied and the gravitational effects of DM on the dynamical evolution of EMRIs were modeled at the Newtonian level. In Ref. [53], the authors generalized Einstein clusters [54, 55] to include horizons, solved Einstein equations sourced by DM halo of Hernquist type [36] with a MBH at its center and obtained an analytical formula for the metric of galaxies harboring MBHs. Exact solutions for the geometry of a MBH immersed in DM halos with different density distributions were then derived [56–58]. With the fully relativistic formalism, it was found that the leading-order correction to the ring-down stage induced by the external matter and fluxes by orbiting particles is a gravitational redshift, and the difference between the numbers of GW cycles accumulated by EMRIs with and without DM halos over one year before the innermost stable circular orbit (ISCO) can reach about 500 [53]. In galaxies harboring MBHs, tidal forces, and geodesic deviation depend on the mass of the DM halo and the typical length scale of the galaxies [59]. Due to the gravitational pull of DM halos, the apsidal precession of the geodesic orbits for EMRIs is strongly affected and even prograde-to-retrograde drift can occur

* daining@hust.edu.cn

† Corresponding author. yggong@hust.edu.cn

‡ zhaoyangedu@hust.edu.cn

§ jiangtong@hust.edu.cn

[60]. In prograde-to-retrograde orbital alterations, GWs show transient frequency phenomena around a critical non-precessing turning point. A fully relativistic formalism to study GWs from EMRIs in a static, spherically symmetric nonvacuum spacetime describing a MBH immersed in generic astrophysical environment was established in Ref. [61], it was shown how the astrophysical environment changes GW emissions and the ability of GW to constrain smaller scale matter distribution around BHs.

The above discussions are based on quasi-circular orbits or eccentric cases without GW reaction. Non-negligible eccentricity in the detector band is possible through dynamical channels, field triples, GW capture and triples near supermassive BHs [62–67], so the inclusion of eccentricity is particularly relevant for EMRIs although the eccentricity decreases due to GW radiation [68–72]. On the other hand, environmental effects are capable of increasing the eccentricity, even a small initial eccentricity can become larger over a long evolving time [46, 50, 70]. The multiple harmonics induced by the eccentricity can break the degeneracy between source parameters which is helpful for the measurement of the position and distance of the GW source [73]. This motivates us to study EMRIs in eccentric orbits. The evolution of EMRIs within DM halos is not only affected by the GW reaction and the gravitational effect of DM halo, but also influenced by the dynamical friction and accretion of the DM medium. When the SCO passes through the DM halo, the gravitational pull from the DM medium slows it down, this effect is called dynamical friction [70, 74]. If the SCO is a small BH, it will accrete the surrounding DM medium around it. The accretion rate can be described by the Bondi-Hoyle-Lyttleton accretion model [75, 76].

In this paper, we study eccentric orbital motions and GWs of EMRIs in galaxies with DM halos. We discuss the combined effects of GW reaction, dynamical friction and accretion on the orbital motion of EMRIs. The paper is organized as follows. In Sec. II, a review of the spacetime of galaxies harboring MBHs is given first, then we discuss the geodesic motion in this spacetime. In Sec. III, we use the "Numerical Kludge" method [69, 77, 78] to calculate GWs from eccentric EMRIs in galaxies with DM halos. To assess the capability of detecting DM halos with LISA, we calculate the mismatch between GWs from EMRIs with and without DM halos along with their signal-to-noise ratios (SNRs). To consider the influence of the degeneracy between the source parameters, we use the Fisher information matrix (FIM) method to estimate the parameter errors in Sec. IV. We draw conclusions in Sec. V. In this paper, we use the units $G = c = 1$.

II. THE MOTIONS OF BINARIES IN THE ENVIRONMENTS OF GALAXIES

The density distribution of a galactic DM halo can be parameterized as [79]

$$\rho(r) = 2^{(\gamma-\alpha)/k} \rho_0 (r/r_0)^{-\alpha} (1 + r^k/r_0^k)^{-(\gamma-\alpha)/k}, \quad (1)$$

where r is the distance to the center of the halo, r_0 is the typical length-scale of a galaxy, ρ_0 is the density of the DM halo at r_0 , and the parameters α , γ , and k describe the type of DM halo depending on the size, mass, and form of the galaxy. For the Navarro, Frenk and White profile [34] which models galaxies with the largest content of DM, $\alpha = 1$, $\gamma = 3$ and $k = 1$. For a dwarf galaxy composed of about a thousand up to several billion stars, the Burkert model with $\alpha = 1$, $\gamma = 3$ and $k = 2$ [80] applies. For the Hernquist-type density distribution [36] describing the Sérsic profiles observed in the bulges and elliptical galaxies, $\alpha = 1$, $\gamma = 4$ and $k = 1$. In this paper, without the loss of generality, we focus on the Hernquist-type density distribution investigated in [53]. Note that the orbital motion and GW waveform will be different for different choices of the DM density profile [56, 81, 82].

The Hernquist-type density distribution can be rewritten as

$$\rho_H = \frac{Mr_0}{2\pi r(r+r_0)^3}, \quad (2)$$

where M is the total mass of the DM halo. For astrophysical scenarios, the compactness of the DM halo M/r_0 is usually small, i.e., $M/r_0 \lesssim 10^{-4}$ [34], and $r_0 = 20$ kpc for the Milky Way [83, 84]. In the galactic environments containing MBHs, the parameter M/r_0 is basically free [53]. Following Ref. [53], the energy-momentum tensor of a galaxy harboring a MBH with the mass M_{BH} is assumed to be

$$T_{\nu}^{\mu} = \text{diag}(-\rho_{\text{DM}}, 0, P_t, P_t), \quad (3)$$

and the spacetime geometry is described by the static, spherically symmetric metric

$$ds^2 = -f(r)dt^2 + \frac{dr^2}{1-2m(r)/r} + r^2(d\theta^2 + \sin^2\theta d\phi^2). \quad (4)$$

Combining Eqs. (3) and (4), Einstein equations become

$$\frac{1}{f(r)} \frac{df(r)}{dr} = \frac{2m(r)}{r(r-2m(r))}, \quad (5)$$

$$\frac{dm(r)}{dr} = 4\pi r^2 \rho_{\text{DM}}(r), \quad (6)$$

$$2P_t = \frac{m(r)\rho_{\text{DM}}(r)}{r-2m(r)}. \quad (7)$$

Dependent on the choice of $\rho_{\text{DM}}(r)$, the mass function $m(r)$ will be different. We assume that the density profile

for a MBH residing at the center of the Hernquist-type distribution (2) is

$$\rho_{\text{DM}} = \frac{Mr_0(1+2M_{\text{BH}}/r_0)(1-2M_{\text{BH}}/r)}{2\pi r(r+r_0)^3}. \quad (8)$$

Obviously, in the absence of the central MBH, the density profile (8) reduces to Eq. (2). At large distances, $r \gg M_{\text{BH}}$, the density profile ρ_{DM} becomes the Hernquist-type distribution (2) for large galaxies with $r_0 \gg M_{\text{BH}}$. If $r_0 \gg r \gg M_{\text{BH}}$, then $\rho_{\text{DM}} \sim (M/r_0)^2/(Mr)$, so the DM density ρ_{DM} is smaller if the compactness M/r_0 is smaller with fixed M , or if M is larger with fixed compactness M/r_0 .

With the choice of the density profile (8), we get the mass function

$$m(r) = M_{\text{BH}} + \frac{Mr^2}{(r_0+r)^2} \left(1 - \frac{2M_{\text{BH}}}{r}\right)^2. \quad (9)$$

The mass function $m(r)$ in Eq. (9) is a combination of the original mass distribution of Hernquist-halo and the mass of the central BH.

Combining Eqs. (5) and (9), we get [53]

$$\begin{aligned} f(r) &= \left(1 - \frac{2M_{\text{BH}}}{r}\right) e^{\Upsilon}, \\ \Upsilon &= -\pi\sqrt{\frac{M}{\xi}} + 2\sqrt{\frac{M}{\xi}} \arctan\left(\frac{r+r_0-M}{\sqrt{M\xi}}\right), \\ \xi &= 2r_0 - M + 4M_{\text{BH}}. \end{aligned} \quad (10)$$

The metric (4) describes a BH spacetime with a horizon at $r = 2M_{\text{BH}}$ and a curvature singularity at $r = 0$, the matter density vanishes at the horizon and the ADM mass of the spacetime is $M + M_{\text{BH}}$. In the absence of DM halo, $M = 0$, the spacetime (4) reduces to Schwarzschild BH with mass M_{BH} . In general astrophysical environments, $M_{\text{BH}} \ll M \ll r_0$. Expanding the function $f(r)$ in Eq. (10) about $M/r_0 = 0$ to the second order we get

$$\begin{aligned} f(r) &\simeq \left(1 - \frac{2M_{\text{BH}}}{r}\right) \left(1 - \frac{2M}{r_0} + \frac{4M^2}{3r_0^2} + \frac{2Mr}{r_0^2}\right) \\ &= \left(1 - \frac{2M_{\text{BH}}}{r}\right) (1 + \lambda + \beta r), \end{aligned} \quad (11)$$

where $\lambda = -2M/r_0 + 4M^2/3r_0^2$ and $\beta = 2M/r_0^2$.

Now, we consider a MBH in the center of a DM halo and a SCO moving on geodesics around the MBH in the equatorial plane ($\theta = \pi/2$). The geodesic equation is

$$\frac{du_\mu}{d\tau} = \frac{1}{2}u^\alpha u^\beta \partial_\mu g_{\alpha\beta}, \quad (12)$$

where $u^\alpha = dr^\alpha/d\tau$, τ is the proper time, and $r^\alpha = (t, r, \theta, \phi)$. Because the spacetime is static and spherically symmetric, from the geodesic equation (12) we obtain two conserved quantities, $u_0 = -E/\mu$ and $u_\phi = L/\mu$,

$$u_0 = -E/\mu = -\sqrt{1+2\varepsilon}, \quad (13)$$

$$u_\phi = L/\mu = h, \quad (14)$$

where E and L represent the orbital energy and angular momentum of the system, respectively, and the reduced mass μ is approximately equal to the mass of the SCO. The radial equation of motion is

$$1 + \left(\frac{dr}{d\tau}\right)^2 \left(1 - \frac{2m(r)}{r}\right)^{-1} + \frac{h^2}{r^2} = \frac{1+2\varepsilon}{f}. \quad (15)$$

For convenience, we introduce the orbital elements, the semi-latus rectum p and the eccentricity e , to parameterize the orbital motion,

$$r = \frac{p}{1 + e \cos \chi}, \quad (16)$$

where χ is a parameter. Rewriting the variables h and ε in terms of p and e , we obtain

$$\begin{aligned} h^2 &= \frac{p R_s (1 + \lambda) + p^3 \beta (1 - e^2)^{-1}}{\left(1 - \frac{R_s}{2p} (3 + e^2)\right) + p \beta \left(1 - \frac{2R_s}{p}\right)} \\ &\times \frac{1}{2(1 + \lambda)}, \end{aligned} \quad (17)$$

$$\varepsilon = -\frac{\frac{R_s}{2p} (1 - e^2) \left(1 - \frac{2R_s}{p}\right) + \lambda \Sigma + \lambda^2 \Delta + \beta Z}{2 \left[\left(1 - \frac{1}{2} \frac{R_s}{p} (3 + e^2)\right) (1 + \lambda) + p \beta \left(\frac{1}{2} - \frac{R_s}{p}\right)\right]} \quad (18)$$

where $R_s = 2M_{\text{BH}}$,

$$\begin{aligned} \Sigma &= -\left(1 - \frac{2R_s}{p}\right) + \frac{R_s}{2p} \left(1 - \frac{4R_s}{p}\right) (1 - e^2), \\ \Delta &= -\left(1 - \frac{2R_s}{p}\right) - \frac{R_s^2}{p^2} (1 - e^2), \\ Z &= -\frac{p(3 + e^2)}{2(1 - e^2)} \left(1 - 2\frac{R_s}{p}\right) - \frac{2R_s^2}{p}. \end{aligned}$$

In terms of χ , Eqs. (13) and (14) become

$$\begin{aligned} \frac{d\phi}{d\chi} &= \left[\frac{1}{2} \frac{R_s}{p} (1 + \lambda) + \frac{1}{2} p \beta (1 - e^2)^{-1}\right]^{\frac{1}{2}} \\ &\times \left\{ \frac{1}{2} \frac{R_s}{p} \left[1 - \frac{R_s}{p} (3 + e \cos \chi)\right] \right. \\ &\left. + \lambda A + \frac{1}{2} \lambda^2 A + \beta B \right\}^{-\frac{1}{2}} J_1, \end{aligned} \quad (19)$$

$$\begin{aligned} \frac{dt}{d\chi} &= \frac{p}{(1 + e \cos \chi)^2} \left\{ \left[1 - (1 + e) \frac{R_s}{p}\right] \right. \\ &\times \left[1 - (1 - e) \frac{R_s}{p}\right] + C \left. \right\}^{\frac{1}{2}} \\ &\times \left[1 - \frac{R_s}{p} (1 + e \cos \chi)\right]^{-1} \\ &\times \left\{ \frac{1}{2} \frac{R_s}{p} \left[1 - \frac{R_s}{p} (3 + e \cos \chi)\right] \right. \\ &\left. + \lambda A + 2\lambda^2 A + \beta B \right\}^{-\frac{1}{2}} J_2, \end{aligned} \quad (20)$$

where

$$\begin{aligned}
A &= \frac{R_s}{p} \left[1 - \frac{R_s}{p} (3 + e \cos \chi) \right], \\
B &= \frac{p}{2(1-e^2)(1+e \cos \chi)} \left\{ 2 \left(1 - \frac{R_s}{p} \right) + \right. \\
&\quad \left[1 - \frac{4R_s}{p} - \left(\frac{R_s}{p} \right)^2 (1-e^2) \right] (1+e \cos \chi) \\
&\quad \left. - \frac{R_s}{p} (1 + \cos^2 \chi) e^2 \right\}, \\
C &= \lambda \left[1 - \frac{1}{2} (3 + e^2) \frac{R_s}{p} \right] + \frac{1}{2} p \beta \left(1 - 2 \frac{R_s}{p} \right) \\
&\quad - (\lambda \Sigma + \lambda^2 \Delta + \beta Z),
\end{aligned}$$

$$\begin{aligned}
J_1 &= \left(1 + \lambda + \frac{\beta p}{1 + e \cos \chi} \right)^{\frac{1}{2}} \left\{ 1 - \frac{2Mp/(1 + e \cos \chi)}{[r_0 + p/(1 + e \cos \chi)]^2} \right. \\
&\quad \left. \times \left[1 - \frac{R_s}{p} (1 + e \cos \chi) \right] \right\}^{-\frac{1}{2}}, \\
J_2 &= \left(1 + \lambda + \frac{\beta p}{1 + e \cos \chi} \right)^{-\frac{1}{2}} \left\{ 1 - \frac{2Mp/(1 + e \cos \chi)}{[r_0 + p/(1 + e \cos \chi)]^2} \right. \\
&\quad \left. \times \left[1 - \frac{R_s}{p} (1 + e \cos \chi) \right] \right\}^{-\frac{1}{2}}.
\end{aligned}$$

Equations. (19) and (20) can be integrated to obtain $\phi(\chi)$ and $t(\chi)$. Taking different compactness and mass for the DM halo, using Cartesian coordinates $(x, y) = (r \cos \phi, r \sin \phi)$ in the equatorial plane, we show the orbits of EMRIs in galaxies with and without DM in Fig. 1. Due to the gravitational force of DM halos, the orbits with DM halos are different from those without DM. From Fig. 1, we see that for the same value of M , the effect of DM halos on the orbital precession is larger if the compactness of the DM halo M/r_0 is bigger. DM halos decrease the orbital precession rates, and they can even reverse the direction of precession if the density of the DM halo ρ_{DM} is large enough. The result of retrograde precessions of the orbital motion in the spacetime (4) is consistent with that found in [60], and the anomalous precessions of binaries in DM environments were also found in [50, 85, 86].

To probe DM halos and study their impact on the orbits of EMRIs, we calculate the time T and the orbital precession $\Delta\phi$ over one cycle when the orbital parameter χ increases by 2π ,

$$T = \int_0^{2\pi} \frac{dt}{d\chi} d\chi, \quad (21)$$

$$\Delta\phi = \int_0^{2\pi} \frac{d\phi}{d\chi} d\chi - 2\pi. \quad (22)$$

Expanding Eqs. (19) and (20) about $R_s/p = 0$ to the second order and substituting the results into Eqs. (21)

and (22), we get

$$\begin{aligned}
T &= 2\pi \sqrt{\frac{2p^3}{R_s}} \frac{1}{(1-e^2)^{3/2}} \left\{ 1 + \frac{3}{2} (1-e^2) \frac{R_s}{p} \right. \\
&\quad + \frac{3}{2} (1-e^2) \left[1 + \frac{5}{4} (1-e^2)^{\frac{1}{2}} \right] \left(\frac{R_s}{p} \right)^2 \\
&\quad + \frac{M}{r_0} + \frac{3(1-e^2)}{2} \frac{MR_s}{r_0 p} + \frac{5M^2}{6r_0^2} \\
&\quad \left. + \frac{Mp}{r_0^2(1-e^2)} \left(e^2 - \frac{11}{2} \right) - \frac{3Mp^2/R_s}{r_0^2(1-e^2)^2} \right\},
\end{aligned} \quad (23)$$

$$\begin{aligned}
\Delta\phi &= 3\pi \frac{R_s}{p} + \frac{3\pi}{8} (18 + e^2) \left(\frac{R_s}{p} \right)^2 \\
&\quad - \frac{6\pi}{1-e^2} \frac{Mp}{r_0^2} \left[1 + \frac{1+e^2+2p/R_s}{3(1-e^2)^{1/2}} \right].
\end{aligned} \quad (24)$$

The terms with M in the above Eqs. (23) and (24) come from DM halos. In the absence of DM, $M = 0$, the above results (23) and (24) recover those for EMRIs with the central MBH being a Schwarzschild BH. The dominant contribution to the period T in Eq. (23) is the first term, so T becomes larger as the semi-latus rectum p increases. However, there are both positive and negative contributions to T from the local DM halos, so the local DM halos may slow down the increase of T as p increases because of the negative contribution in the last term in Eq. (23) and the presence of DM halos helps the increase of T with p if the last negative contribution is negligible. From Eq. (24), it is easy to understand that the presence of DM halo decreases the orbital precession and even retrogrades the orbital precession if the local density of DM halos $\rho_{\text{DM}} \sim M/r_0^2$ is sufficiently large that the third term dominates over the first two terms. For larger orbits, i.e., the semi-latus rectum p is larger, the orbital precession decreases and the prograde precession decreases faster in the presence of DM halos because the third term due to DM halos in Eq. (24) becomes bigger. In the presence of DM halos, the prograde-to-retrograde precession transition happens at some critical value of p , and then the retrograde precessions become bigger if p is larger. Choosing different values for the compactness M/r_0 and the total mass of DM halos M and using Eqs. (23) and (24), we plot the results of the period T and the orbital precession $\Delta\phi$ versus the semi-latus rectum p in Fig. 2. As expected, the orbital period T increases with p , the prograde precessions decrease with p and DM halos accelerate the decrease. For the case of $r_0 = 10^2 M$ and $M = 10^2 M_{\text{BH}}$, the periapsis shifts change from prograde precessions to retrograde precessions at $p = 120 M_{\text{BH}}$ and the retrograde precession increases with p when $p \gtrsim 120 M_{\text{BH}}$.

From the above discussions, we see that the orbital motions of EMRIs are influenced by DM halos, and we expect that the effects of local DM halos will leave imprints on GWs so that we can probe local DM halos through the observations of GWs emitted from EMRIs.

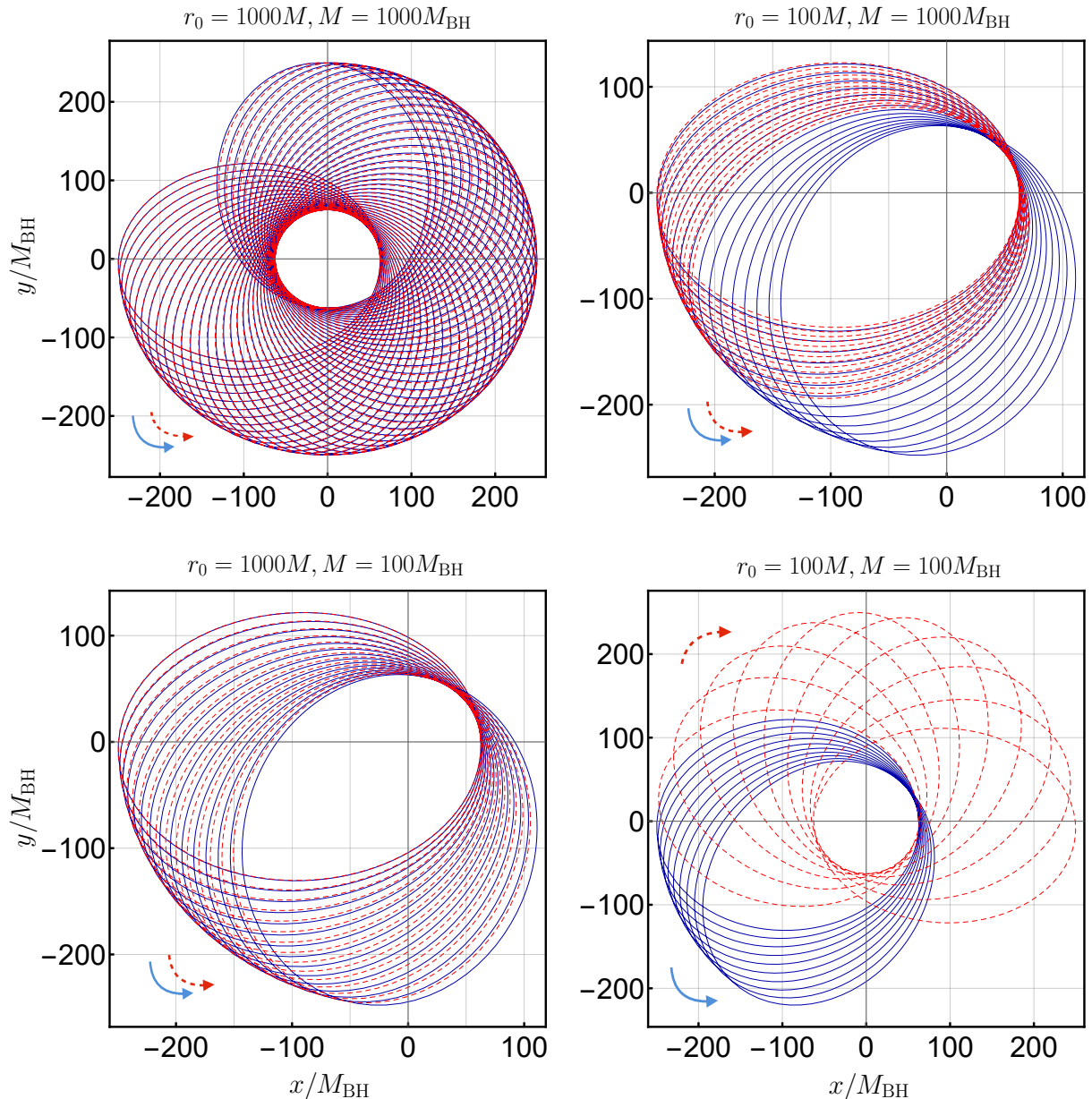


FIG. 1. The orbits of EMRIs in galaxies with and without DM halos. The mass of the MBH is set as $M_{\text{BH}} = 10^6 M_{\odot}$, the eccentricity $e = 0.6$, and the semi-latus rectum $p = 200M_{\text{BH}}$. We take the compactness M/r_0 as 10^{-2} and 10^{-3} , and the mass of the halo M as $10^2 M_{\text{BH}}$ and $10^3 M_{\text{BH}}$. The red dashed lines show the trajectories with DM and the blue solid lines show the orbits without DM. The arrows represent the directions of orbital precessions.

III. GWS OF EMRIS IN THE ENVIRONMENTS OF GALAXIES

A. Orbital evolution

In this section, we take the SCO as a BH. When the small BH passes through the DM medium, the gravitational pull from DM particles decelerates the small BH. This effect is called the dynamical friction and the force

$$\mathbf{f}_{\text{DF}} = -\frac{4\pi\mu^2\rho_{\text{DM}}\ln\Lambda}{v^3}\mathbf{v}, \quad (25)$$

where \mathbf{v} is the velocity of the small BH, and we choose the Coulomb logarithm $\ln\Lambda = 3$ [41].

Combining Eqs. (16), (19), (20), and (25), the energy and the angular momentum loss rates caused by the dy-

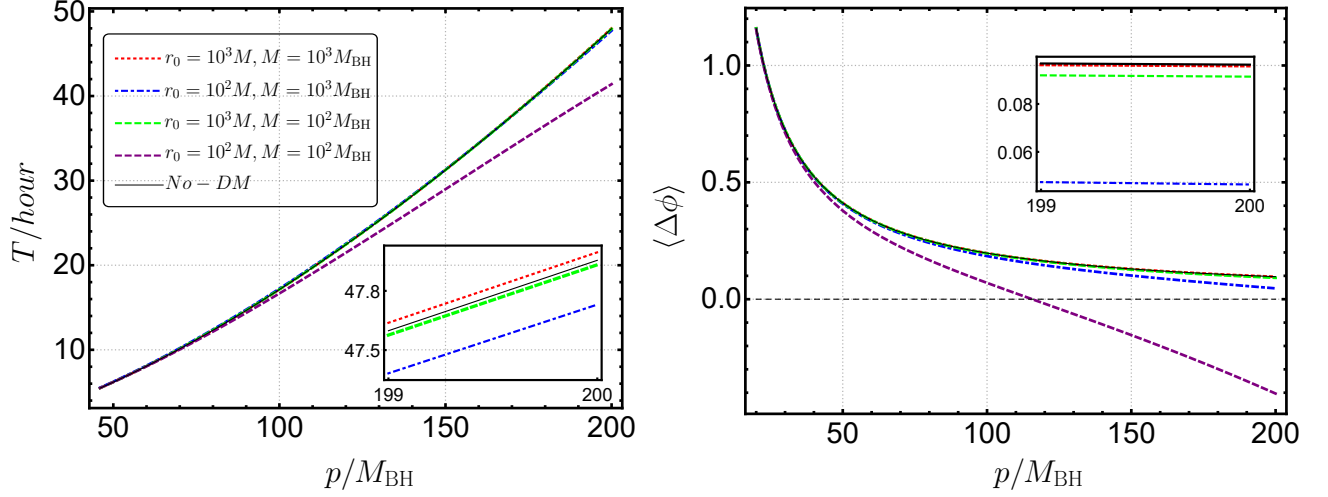


FIG. 2. The results of the orbital period and precession for EMRIs in galaxies with and without DM. The mass of the central MBH is set as $M_{\text{BH}} = 10^6 M_{\odot}$ and the eccentricity $e = 0.6$. We take the compactness M/r_0 as 10^{-2} and 10^{-3} , and the total mass M of the halo as $10^3 M_{\text{BH}}$, $10^2 M_{\text{BH}}$ and $M = 0$. The inserts show the evolution in a short time period.

dynamic frictions are

$$\left(\frac{dE}{dt}\right)_{\text{DF}} = -\frac{6\sqrt{2}\mu^2(1-R_s/p)^{3/2}}{\sqrt{R_s}(p-(1+e\cos\chi)R_s)}\frac{M}{r_0^2}K_1 \quad (26)$$

$$\times \sqrt{(p-(1-e)R_s)(p-(1+e)R_s)},$$

$$\left(\frac{dL}{dt}\right)_{\text{DF}} = -\frac{12\mu^2\sqrt{p}(p-R_s)^{5/2}}{R_s(p-R_s-eR_s\cos\chi)^{5/2}}\frac{M}{r_0^2}K_2 \quad (27)$$

$$\times (p+(-1+e)R_s)(p-(1+e)R_s),$$

where

$$K_1 = \left[(p-R_s)(1+e\cos\chi)^4 + e^2(p-3R_s-eR_s\cos\chi)\sin^2\chi \right]^{-1/2},$$

$$K_2 = \left[(p-R_s)(1+e\cos\chi)^4 + e^2(p-3R_s-eR_s\cos\chi)\sin^2\chi \right]^{-3/2}.$$

When moving in the DM halo, the small BH can accrete the surrounding DM medium. This effect can be modeled by the Bondi-Hoyle accretion [40, 75, 76]

$$\dot{\mu} = \frac{4\pi\rho_{\text{DM}}\mu^2}{(v^2+c_s^2)^{3/2}}, \quad (28)$$

where $c_s = \sqrt{\delta P_t/\delta\rho}$ is the sound speed, and the overdot indicates differentiation with respect to t . Note that the effects of DF and accretion in Eqs. (25) and (28) are Newtonian estimated.

It was shown in Refs. [87, 88] that the accretion does not result in the exchange of orbital angular momentum,

i.e., $(dL/dt)_{\text{acc}} = 0$. The variation of orbital energy due to the mass increase is

$$\left(\frac{dE}{dt}\right)_{\text{acc}} = \frac{\dot{\mu}}{\mu}E - \dot{\mu}v^2, \quad (29)$$

where E is the orbital energy defined in Eq. (13).

The energy and angular momentum loss rates due to GW emissions are described by the quadrupole formula

$$\left(\frac{dE}{dt}\right)_{\text{GW}} = -\frac{1}{5}\ddot{\mathcal{I}}^{jk}\ddot{\mathcal{I}}^{jk}, \quad (30)$$

$$\left(\frac{dL_i}{dt}\right)_{\text{GW}} = -\frac{2}{5}\epsilon_{ijk}\ddot{\mathcal{I}}^{jl}\ddot{\mathcal{I}}^{kl}, \quad (31)$$

where \mathcal{I}^{jk} is the symmetric-traceless part of the mass quadrupole. Using the results for the orbital motions of EMRIs within DM halos obtained above and considering the variation of the mass, we get the leading order energy and angular momentum fluxes of the GW reaction

$$\left(\frac{dE}{dt}\right)_{\text{GW}} = -\frac{4M_{\text{BH}}^5\mu^2}{15p^5}f_1(e,\phi)\left(1-\frac{6M}{r_0}\right) + \frac{4M_{\text{BH}}^{9/2}\dot{\mu}\mu}{5p^{7/2}}f_2(e,\phi)\left(1-\frac{5M}{r_0}\right) + \frac{6M_{\text{BH}}^4\dot{\mu}^2}{5p^2}f_3(e,\phi)\left(1-\frac{4M}{r_0}\right), \quad (32)$$

$$\left(\frac{dL}{dt}\right)_{\text{GW}} = -\frac{4M_{\text{BH}}^{9/2}\mu^2}{5p^{7/2}}g_1(e,\phi)\left(1-\frac{5M}{r_0}\right) - \frac{24M_{\text{BH}}^4\dot{\mu}\mu}{5p^2}g_2(e,\phi)\left(1-\frac{4M}{r_0}\right) + \frac{24M_{\text{BH}}^{7/2}\dot{\mu}^2}{5p^{1/2}}g_3(e,\phi)\left(1-\frac{3M}{r_0}\right), \quad (33)$$

where

$$\begin{aligned} f_1(e, \phi) &= (1 + e \cos \phi)^4 (24 + 13e^2 \\ &\quad + 48e \cos \phi + 11e^2 \cos 2\phi), \\ f_2(e, \phi) &= (1 + e \cos \phi)^2 (18 + 13e^2 + 40e \cos \phi \\ &\quad + 9e^2 \cos 2\phi), \\ f_3(e, \phi) &= 12 + 20e^2 + 4e^4 + (36e + 17e^3) \cos \phi \\ &\quad + 20e^2 \cos 2\phi + 3e^3 \cos 3\phi, \end{aligned}$$

and

$$\begin{aligned} g_1(e, \phi) &= (1 + e \cos \phi)^3 (8 + e^2 \\ &\quad + 12e \cos \phi + 3e^2 \cos 2\phi), \\ g_2(e, \phi) &= (1 + e \cos \phi)^2 \sin \phi, \\ g_3(e, \phi) &= 2 + e^2 + 3e \cos \phi. \end{aligned}$$

In Eqs. (32) and (33), the factors $(1 - nM/r_0)$ are the corrections from DM halos around the central MBH, and the terms with $\dot{\mu}$ are the contributions from the mass variation of the small BH. Note that the losses of energy and angular momentum due to the GW reaction depend on the compactness M/r_0 , and the energy flux becomes smaller if the compactness is larger. In the absence of local DM halos, $M = 0$, Eqs. (32) and (33) reduce to the results for eccentric binaries in the vacuum [89, 90].

The energy and angular momentum fluxes with the orbital period averaging are

$$\left\langle \frac{dE}{dt} \right\rangle = \frac{1}{T} \int_0^T \frac{dE}{dt} dt = \frac{1}{T} \int_0^{2\pi} \frac{dE}{dt} \frac{dt}{d\phi} d\phi, \quad (34)$$

$$\left\langle \frac{dL_z}{dt} \right\rangle = \frac{1}{T} \int_0^T \frac{dL_z}{dt} dt = \frac{1}{T} \int_0^{2\pi} \frac{dL_z}{dt} \frac{dt}{d\phi} d\phi. \quad (35)$$

Inserting Eqs. (26), (27), (29), (32), and (33) into Eqs. (34) and (35), we obtain the averaged energy and angular momentum fluxes of the dynamical friction, accretion, and GW reaction. We show the averaged energy and angular momentum fluxes of the dynamical friction, accretion, and GW reaction with different parameters for DM halos in Fig. 3.

In the left panels of Fig. 3, we graph the energy fluxes at different p for different M and r_0 , and the angular momentum fluxes are shown in the right panels. As expected from Eq. (29), the energy fluxes of the accretion are positive. The energy fluxes of the GW reaction dominate when the small BH is close to the central MBH ($p \lesssim 15M_{\text{BH}}$), and the energy fluxes of the dynamical friction dominate when $p \gtrsim 25M_{\text{BH}}$. We also see that the angular momentum fluxes of the GW reaction are much bigger than the dynamical friction when $p \lesssim 15M_{\text{BH}}$, and the angular momentum fluxes of the dynamical friction are bigger than the GW reaction when $p \gtrsim 25M_{\text{BH}}$. From Eqs. (32) and (33), we see that the fluxes of the GW reaction are inversely proportional to p^δ , so the fluxes of

the GW reaction are larger when the orbit of the binary is smaller. From Eqs. (25) and (28), we see that $\dot{\mu}$ and the dynamical friction are proportional to v^{-2} . Since the velocity is smaller in larger orbits, thus the effects of the accretion and dynamical friction are larger when $p \gtrsim 25M_{\text{BH}}$ and smaller when $p \lesssim 15M_{\text{BH}}$.

The energy and angular momentum fluxes of the GW reaction shown in the upper and lower panels in Fig. 3 are almost the same, and the effects of the accretion and dynamical friction shown in the upper and middle panels in Fig. 3 are almost the same. This is because the compactness of the DM halos M/r_0 chosen in the upper and lower panels is the same, and the effect of DM halo on the energy and angular momentum fluxes of the GW reaction is mainly manifested through M/r_0 . since the same values of M/r_0^2 are chosen in the upper and middle panels, and the effects of the dynamical friction and accretion are mainly related to the DM density $\rho_{\text{DM}} \sim M/r_0^2$, the energy fluxes due to the dynamical friction and accretion shown in the upper and middle panels are almost the same.

The changes of orbital energy and angular momentum due to the net effect of the dynamical friction, accretion and GW reaction can be written as

$$\begin{aligned} \left(\frac{dE}{dt} \right)_{\text{orb}} &= \frac{dE}{dp} \frac{dp}{dt} + \frac{dE}{de} \frac{de}{dt} + \frac{dE}{d\mu} \frac{d\mu}{dt} \\ &= \left\langle \frac{dE}{dt} \right\rangle_{\text{GW}} + \left\langle \frac{dE}{dt} \right\rangle_{\text{DF}} \\ &\quad + \left\langle \frac{dE}{dt} \right\rangle_{\text{ACC}}, \end{aligned} \quad (36)$$

$$\begin{aligned} \left(\frac{dL}{dt} \right)_{\text{orb}} &= \frac{dL}{dp} \frac{dp}{dt} + \frac{dL}{de} \frac{de}{dt} + \frac{dL}{d\mu} \frac{d\mu}{dt} \\ &= \left\langle \frac{dL}{dt} \right\rangle_{\text{GW}} + \left\langle \frac{dL}{dt} \right\rangle_{\text{DF}}. \end{aligned} \quad (37)$$

By combining the exact geodesic motion with the energy and angular momentum fluxes of DF, accretion, and GWs, we can obtain the orbital evolution of EMRIs in DM halos. Compared to the Teukolsky approach, the method we use here is less accurate but faster to calculate and more precise than the Newtonian method [77]. Inserting Eqs. (13), (14), (26), (27), (29), (32) and (33) into Eqs. (36) and (37), and numerically calculating the evolution of the orbital parameters p , e and μ due to the combined effects of the dynamical friction, accretion, and GW reaction, we get the results as shown in Fig. 4. From Fig. 4 we see that EMRIs immersed in DM halos evolve more slowly. The larger the compactness M/r_0 is, the more evolution time it takes. The presence of DM halos also slows down the decrease rate of the eccentricity. Near $p_0 = 6.2M_{\text{BH}}$, the orbital eccentricity of EMRIs increases sharply, which is a significant feature of eccentric EMRIs [77]. In the one-year evolution, the mass of the small BH increases very little and the mass increases less with smaller ρ_{DM} .

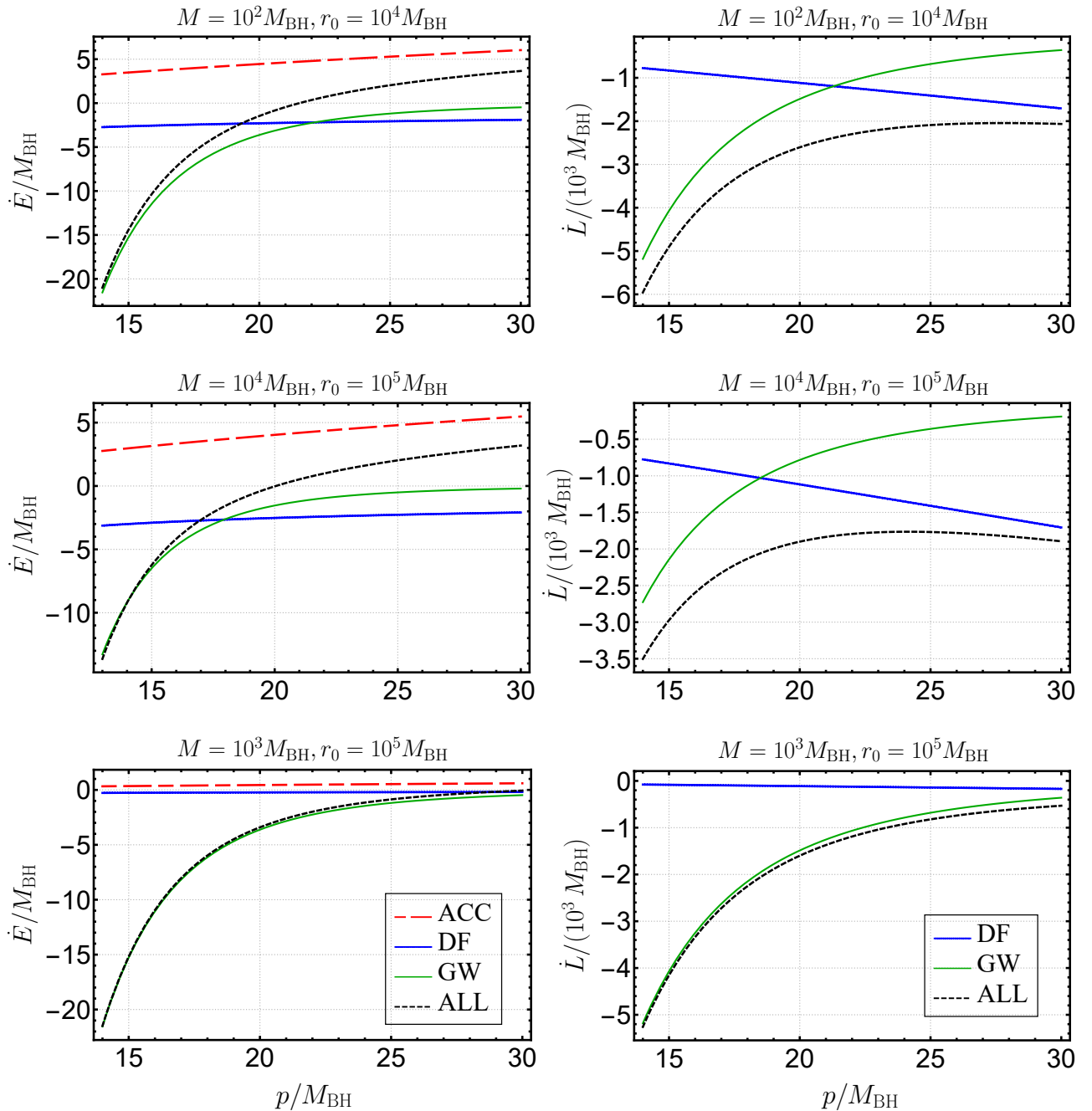


FIG. 3. The averaged energy and angular momentum fluxes from the dynamical friction, accretion effect and GW reaction at different p . The symbols "ACC", "DF", and "GW" represent the accretion, dynamical friction and GW reaction, respectively. "ALL" means the combined net effect of the dynamical friction, accretion and GW reaction. The mass of the central MBH is chosen as $M_{\text{BH}} = 10^6 M_{\odot}$, the mass of the small BH is $\mu = 10 M_{\odot}$ and the eccentricity is chosen as $e = 0.1$.

B. Gravitational waveforms analysis

As discussed above, the effects of DM halos will be manifested in GW waveforms. The quadrupole formula of GWs is

$$h^{jk} = \frac{2}{d_L} \ddot{I}^{jk}, \quad (38)$$

where d_L is the luminosity distance between the detector and the source, and I_{jk} is the quadrupole moment of EMRIs. The plus and cross tensor modes h_+ and h_{\times} in

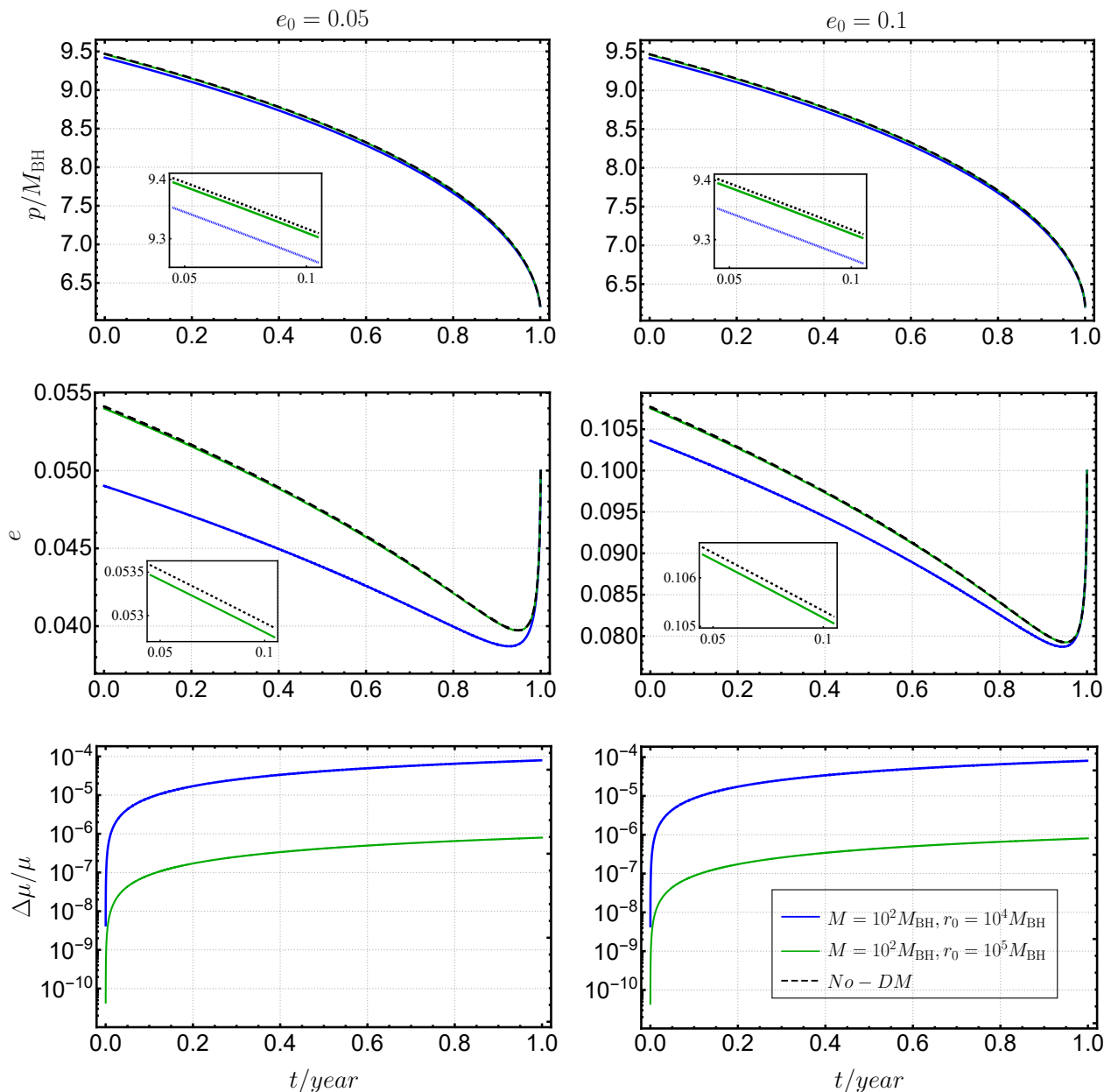


FIG. 4. The evolution of the orbital parameters $p(t)$, $e(t)$, and $\mu(t)$. We choose the orbital evolution over one year before $p_0 = 6.2M_{\text{BH}}$, with initial eccentricity values of $e_0 = 0.05$ and 0.1 . The mass of the central MBH is chosen as $M_{\text{BH}} = 10^6 M_{\odot}$, the mass of the SCO is $\mu_0 = 10M_{\odot}$ and we consider two different values for the compactness of the DM halos, $M/r_0 = 10^{-2}$ and 10^{-3} . The black dashed lines correspond to the cases without DM.

the transverse-traceless gauge are given by

$$h_+ = \frac{1}{2} \left(e_X^j e_X^k - e_Y^j e_Y^k \right) h_{jk}, \quad (39)$$

$$h_{\times} = \frac{1}{2} \left(e_X^j e_Y^k + e_Y^j e_X^k \right) h_{jk}, \quad (40)$$

where e_X and e_Y are the orthonormal vectors in the plane that are perpendicular to the direction from the detector to the GW source. Plugging the results for the orbital evolution obtained above into Eq. (38), we numerically

calculate the time-domain GW waveforms. The time-domain plus-mode GW waveforms for EMRIs with and without DM halos are shown in Fig. 5. From Fig 5, we see that initially the difference between GW waveforms with and without DM halos is negligible. One year later, the two waveforms for EMRIs with and without DM halos are quite different.

To quantify the impact of DM halo environments on the dephasing of GW waveforms, we calculate the number of orbital cycles accumulated from initial time t_i to

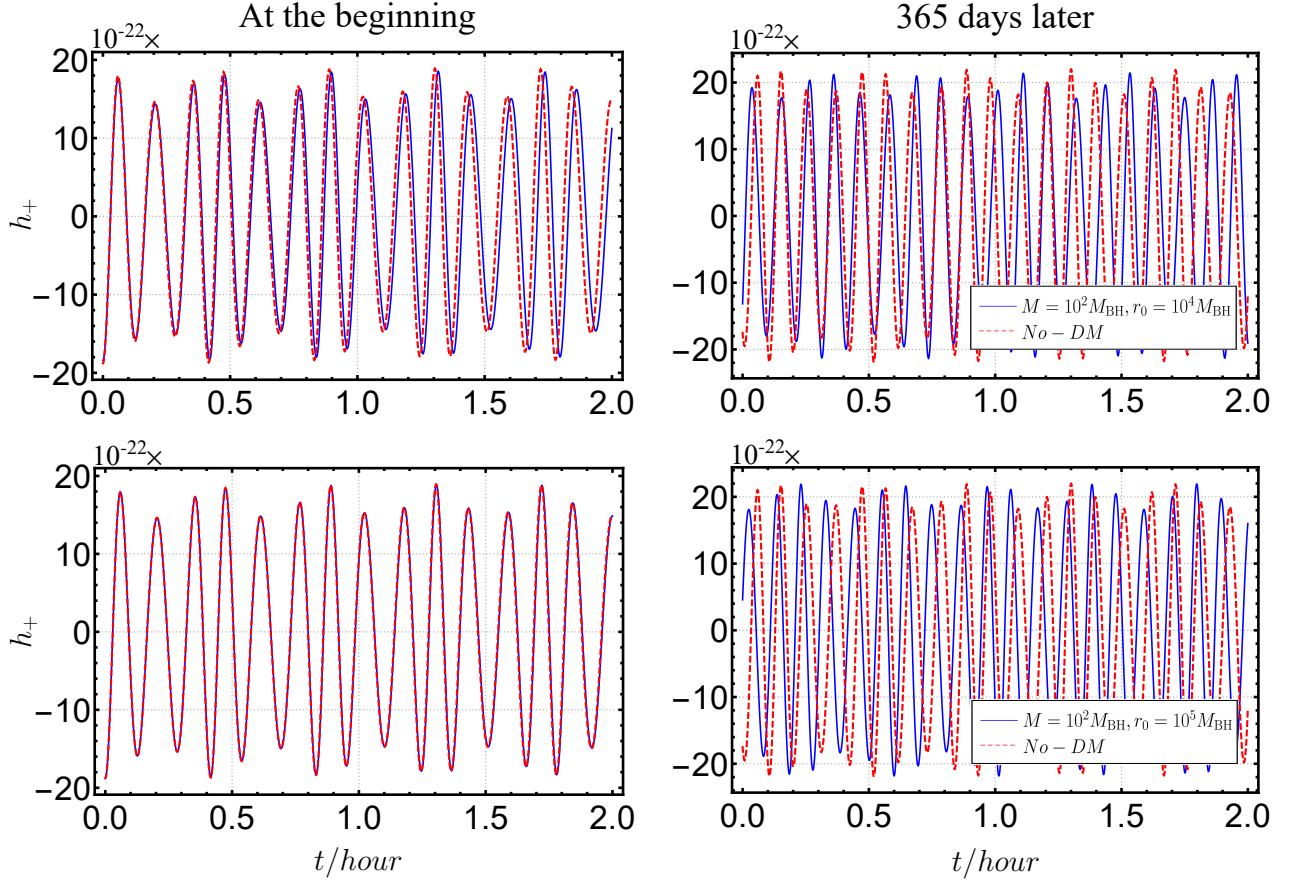


FIG. 5. The time-domain plus mode GW waveforms for EMRIs with and without DM halos. The mass of the central MBH is $M_{\text{BH}} = 10^6 M_{\odot}$, the mass of the SCO is $\mu = 10 M_{\odot}$, the total mass of DM halos $M = 10^2 M_{\text{BH}}$, the inclination angle $\iota = \pi/6$, the luminosity distance $d_L = 1$ Gpc, the initial longitude of the pericenter $\omega_0 = 0$, and the initial eccentricity $e_0 = 0.1$ at $p_0 = 10 M_{\text{BH}}$. $M = 0$ corresponds to the case without DM halos. The left panels show the initial waveforms. The right panels show the waveforms after one year. The top panels are for $M/r_0 = 10^{-2}$, and the bottom panels are for $M/r_0 = 10^{-3}$.

the final time t_f [72, 91, 92]

$$\mathcal{N}(t) = \int_{t_i}^{t_f} \dot{\phi}(t) dt. \quad (41)$$

Over one-year evolution ($t_f - t_i = 1$ year) starting from the time t_i when the orbital period $T_0 = 2\pi\sqrt{(5R_s)^3/M_{\text{BH}}}$, the numbers of orbital cycles accumulated for EMRIs with and without DM halos are \mathcal{N}_{DM} and \mathcal{N}_0 , respectively. In Fig. 6, we show the difference between the number of orbital cycles with and without DM halos accumulated over one year, $\Delta\mathcal{N} = \mathcal{N}_{\text{DM}} - \mathcal{N}_0$. Following [93], we choose $\Delta\mathcal{N} \sim 1$ rad as the threshold for a detectable dephasing. Note that this threshold cannot be taken as a sufficient condition for detectability. The results show that the compactness can be detected as small as $M/r_0 \lesssim 10^{-5}$, and eccentric orbits can detect smaller compactness than circular orbits.

To distinguish the waveforms more accurately, we calculate the mismatch between GW signals emitted from EMRIs with and without DM halos. Given two signals

$h_1(t)$ and $h_2(t)$, the inner product ($h_1|h_2$) is defined as

$$(h_1|h_2) = 2 \int_0^{+\infty} \frac{\tilde{h}_1(f)\tilde{h}_2^*(f) + \tilde{h}_2(f)\tilde{h}_1^*(f)}{S_n(f)} df, \quad (42)$$

where $\tilde{h}(f)$ is the Fourier transformation of the time-domain signal $h(t)$, \tilde{h}^* denotes the complex conjugate of \tilde{h} , and the SNR for the signal h is $\rho = \sqrt{(h|h)}$. For LISA, the one-side noise power spectral density is [94]

$$S_n(f) = \frac{S_x}{L^2} + \frac{2S_a [1 + \cos^2(2\pi fL/c)]}{(2\pi f)^4 L^2} \times \left[1 + \left(\frac{4 \times 10^{-4} \text{Hz}}{f} \right) \right], \quad (43)$$

where $\sqrt{S_a} = 3 \times 10^{-15} \text{ m s}^{-2}/\text{Hz}^{1/2}$ is the acceleration noise, $\sqrt{S_x} = 1.5 \times 10^{-11} \text{ m}/\text{Hz}^{1/2}$ is the displacement noise, and $L = 2.5 \times 10^6 \text{ km}$ is the arm length of LISA [8]. The overlap between two GW signals is [78]

$$\mathcal{O}(\tilde{h}_1, \tilde{h}_2) = \frac{(\tilde{h}_1|\tilde{h}_2)}{\sqrt{(\tilde{h}_1|\tilde{h}_1)(\tilde{h}_2|\tilde{h}_2)}}, \quad (44)$$

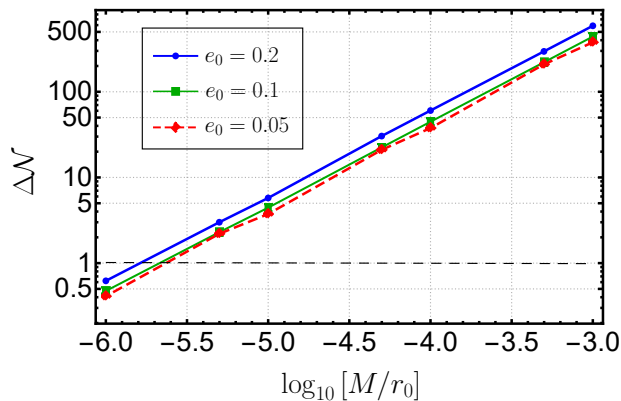


FIG. 6. The difference between the orbital cycles with and without DM halos $\Delta\mathcal{N}(t)$ accumulated over one-year evolution for different compactness values of DM halos. The mass of the central MBH is $M_{\text{BH}} = 10^6 M_{\odot}$, the initial mass of the SCO is $\mu_0 = 10 M_{\odot}$ and the mass of DM halos is $M = 10^2 M_{\text{BH}}$. The initial eccentricity values are chosen as 0.05, 0.1 and 0.2. We take the initial semi-latus rectum p_0 at the position where the orbital period $T_0 = 2\pi\sqrt{(5R_s)^3/M_{\text{BH}}}$. The black dashed line corresponds to $\Delta\mathcal{N} = 1$ rad.

and the mismatch between two signals is defined as

$$\text{Mismatch} = 1 - \mathcal{O}_{\max}(\tilde{h}_1, \tilde{h}_2), \quad (45)$$

where the maximum is evaluated with respect to time and phase shifts. The mismatch is zero if two signals are identical. Two signals are considered experimentally distinguishable if their mismatch is larger than $d/(2\text{SNR}^2)$ [95, 96], where $d = 13$ is the number of intrinsic parameters of the GW source. Considering EMRIs with masses $(10^6 + 10)M_{\odot}$ at $d_L = 1$ Gpc and the integration time of one year before the coalescence, we calculate the mismatch between GW waveforms with and without DM halos and the results with LISA are shown in Fig. 7. The SNR is about 32 for the GW signals from EMRIs considered above. The initial eccentricity e_0 is chosen at $p_0 = 6.3M_{\text{BH}}$. As shown in Fig. 7, if the compactness of the DM halo M/r_0 is larger, then the mismatch between GW waveforms with and without DM halos is bigger, i.e., more compact DM halos can be detected more easily with LISA. Again, eccentric orbits can detect smaller compactness. Therefore, we can use GWs from EMRIs within the environments of galaxies to test the existence of DM halos and detect the compactness of halos with M/r_0 as small as 10^{-5} .

IV. PARAMETER ESTIMATION FOR CIRCULAR EMRIS

To study degeneracies among the source parameters and assess the detector's capacity to constrain the compactness, we perform parameter estimations with the FIM method [97, 98].

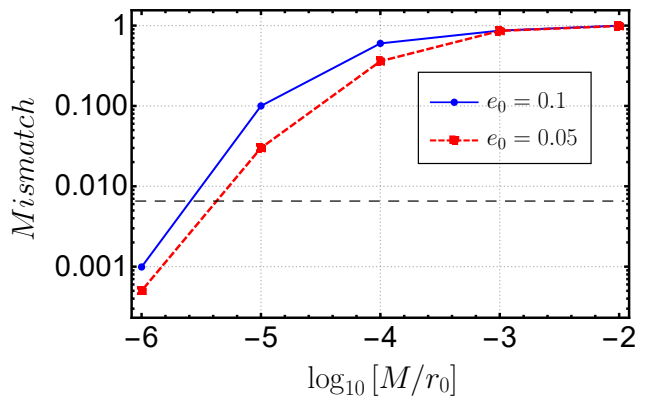


FIG. 7. The results of the mismatch between GW waveforms with and without DM halos for different compactness M/r_0 and initial eccentricity e_0 . The black dashed line corresponds to the threshold $d/(2\text{SNR}^2) \approx 0.007$.

For the GW signal h , the FIM is defined as

$$\Gamma_{ij} = \left(\frac{\partial h}{\partial \xi^i} \middle| \frac{\partial h}{\partial \xi^j} \right), \quad (46)$$

where ξ^i denotes the source parameter. The statistical error on ξ^i is

$$\sigma_i = \Sigma_{ii}^{1/2}, \quad (47)$$

and the correlation coefficient between the parameters ξ^i and ξ^j is

$$c_{ij} = \Sigma_{ij} / (\sigma_i \sigma_j), \quad (48)$$

where $\Sigma_{ij} = (\Gamma^{-1})_{ij}$ is the inverse of the FIM. Because of the triangle configuration of the space-based GW detector, the detector can be regarded as a network of two L-shaped detectors [99], so the total SNR is the sum of the SNRs of two L-shaped detectors,

$$\rho = \sqrt{\rho_1^2 + \rho_2^2} = \sqrt{(s_1|s_1) + (s_2|s_2)}, \quad (49)$$

where s_1 and s_2 denote the signals detected by the two L-shaped detectors, respectively. The total covariance matrix of the source parameters is obtained by inverting the sum of the Fisher matrices, and the parameter error is

$$\sigma_i^2 = (\Gamma_1 + \Gamma_2)_{ii}^{-1}. \quad (50)$$

Taking the Newtonian gravity and dynamical friction of DM halos into account, analytical waveforms of EMRIs with DM halos in quasi-circular orbits were derived in [41] under the stationary phase approximation [97, 100]. Following the approach in [101, 102], we use the FIM method to estimate the parameter error numerically. The GW waveforms of EMRIs in quasi-circular orbits are

$$h_+ = \frac{4\mu(t)\Omega(t)^{2/3}M_{\text{BH}}^{2/3}}{d_L} \frac{1 + \cos^2\iota}{2} \cos[2\varphi(t)] \times \left(1 - \frac{4M}{3r_0} \right), \quad (51)$$

$$h_{\times} = \frac{4\mu(t)\Omega(t)^{2/3}M_{\text{BH}}^{2/3}}{d_L} \cos \iota \sin [2\varphi(t)] \times \left(1 - \frac{4M}{3r_0}\right), \quad (52)$$

where $\Omega(t) = d\varphi/dt$ is the orbital frequency, the orbital phase $\varphi(t)$ is

$$\varphi(t) = \varphi_c + \int_0^t \Omega(t)dt, \quad (53)$$

and φ_c is the initial orbital phase at $t = 0$. Combining Eqs. (19), (20), (36), (37) and (53) for $e_0 = 0$, we can obtain $\mu(t)$, $\Omega(t)$, and $\varphi(t)$ numerically.

The GW strain measured by the detector is

$$h(t) = h_{+}(t)F^{+}(t) + h_{\times}(t)F^{\times}(t), \quad (54)$$

where the interferometer pattern functions $F^{+}(t)$ and $F^{\times}(t)$ can be expressed in terms of the source orientation (θ_s, ϕ_s) and the direction of the angular momentum (θ_1, ϕ_1) . Because of the orientation dependence, GW signals are modulated due to the orbital motion [78, 101]. Removing the extrinsic parameters $\{\theta_s, \phi_s, \theta_1, \phi_1, d_L\}$,

the source parameters related to the evolution of EMRIs within DM halos are

$$\hat{\xi} = \{\ln M_{\text{BH}}, \ln \mu_0, \ln M_{\text{halo}}, \ln r_0, r_c, \varphi_c\}, \quad (55)$$

where μ_0 , r_c , and φ_c are the mass of the SCO, the orbital radius and the orbital phase at $t = 0$, respectively. Combining Eqs. (46), (47), (50), and (54), we estimate the errors of the parameters $\hat{\xi}$.

We take one year of observation time before the ISCO and fix the SNR to be $\rho = 30$ [101, 103]. The source and orbital orientations are fixed as $\theta_s = \pi/3$, $\phi_s = \pi/2$, $\theta_1 = \pi/4$ and $\phi_1 = \pi/4$. The initial orbital phase $\varphi_c = 0$, and r_c is adjusted to experience one-year adiabatic evolution before the ISCO. For LISA, the lower and upper cutoff frequencies are $f_{\text{low}} = 10^{-4}$ Hz and $f_{\text{high}} = 1$ Hz [104], so the lower and upper limits of the integration are chosen as $f_{\text{ini}} = \text{Max}(f_{\text{low}}, f_{1\text{yr}})$ and $f_{\text{end}} = \text{Min}(f_{\text{high}}, f_{\text{ISCO}})$, respectively. $f_{1\text{yr}}$ is the GW frequency at one year before the ISCO, and f_{ISCO} is the frequency at the ISCO. We show the estimated parameter errors of EMRIs with the numerical waveforms in Table I. The probability distribution obtained from the FIM approach for the parameters of EMRIs are shown in Figs. 8, 9, and 10.

$\sigma(\ln r_0)$	$\sigma(\ln M)$	$\sigma(\ln M_{\text{BH}})$	$\sigma(\ln \mu_0)$	$\sigma(r_c)/R_s$	$\sigma(\varphi_c)$	M/r_0	$M/r_0^2 (M_{\text{BH}}^{-1})$
0.00527	0.00618	0.000127	0.00139	0.000527	0.0607	10^{-1}	10^{-6}
0.0472	0.0910	0.000444	0.00149	0.00208	0.0566	10^{-2}	10^{-6}
0.0749	0.129	0.000577	0.00193	0.00270	0.0554	10^{-2}	10^{-7}

TABLE I. The estimated errors of the parameters of GW signals from EMRIs within DM halos with LISA. The mass of the central MBH is $10^6 M_{\odot}$, and the mass of the small BH is $10 M_{\odot}$. The DM halo parameters M/r_0 and M/r_0^2 are listed in the last two columns. The halo parameters (M, r_0) for the three rows are $(10^4 M_{\text{BH}}, 10^5 M_{\text{BH}})$, $(10^2 M_{\text{BH}}, 10^4 M_{\text{BH}})$ and $(10^3 M_{\text{BH}}, 10^5 M_{\text{BH}})$, respectively.

Comparing the results in the second and third rows in Table I, we see that the estimated errors of the parameters (especially $\sigma(\ln r_0)$ and $\sigma(\ln M)$) decrease as the halo density M/r_0^2 increases when the halo compactness remains the same. Comparing the results in the first and second rows in Table I, we see that the increase of the halo compactness M/r_0 can make the error of the parameters decrease when M/r_0^2 remains the same. When M/r_0 changes from 10^{-2} to 10^{-1} , the errors of $\ln M$ and $\ln r_0$ are reduced by almost an order of magnitude. Therefore, larger halo compactness M/r_0 and halo density M/r_0^2 decrease the estimated errors of the parameters and improve the detection accuracy for DM halos. Comparing Figs. 8 and 9, we find that the correlations between $\ln r_0$ and the other parameters, as well as those between $\ln M$ and the other parameters, decrease when M/r_0 changes from 10^{-2} to 10^{-1} . The differences in the correlations between the parameters in Figs. 9 and 10 are not significant, probably because the dependence on the halo

density M/r_0^2 is not strong. Therefore, larger halo compactness is likely to reduce the correlations between the parameters and help to break the degeneracy between the parameters.

V. CONCLUSIONS AND DISCUSSIONS

Using the analytic, static, and spherically symmetric metric for a Schwarzschild BH immersed in DM halos with the Hernquist-type density distribution, we derive analytic formulas for the orbital period and orbital precession of eccentric EMRIs within the environment of DM halos. The results show that the presence of the DM halo retards the orbital precession and even retrogrades the orbital precession if the local density of DM halos $\rho_{\text{DM}} \sim M/r_0^2$ is sufficiently large. For larger orbits, the retrograde precessions decrease faster in the presence of DM halos. With DM halos, the retrograde-to-prograde

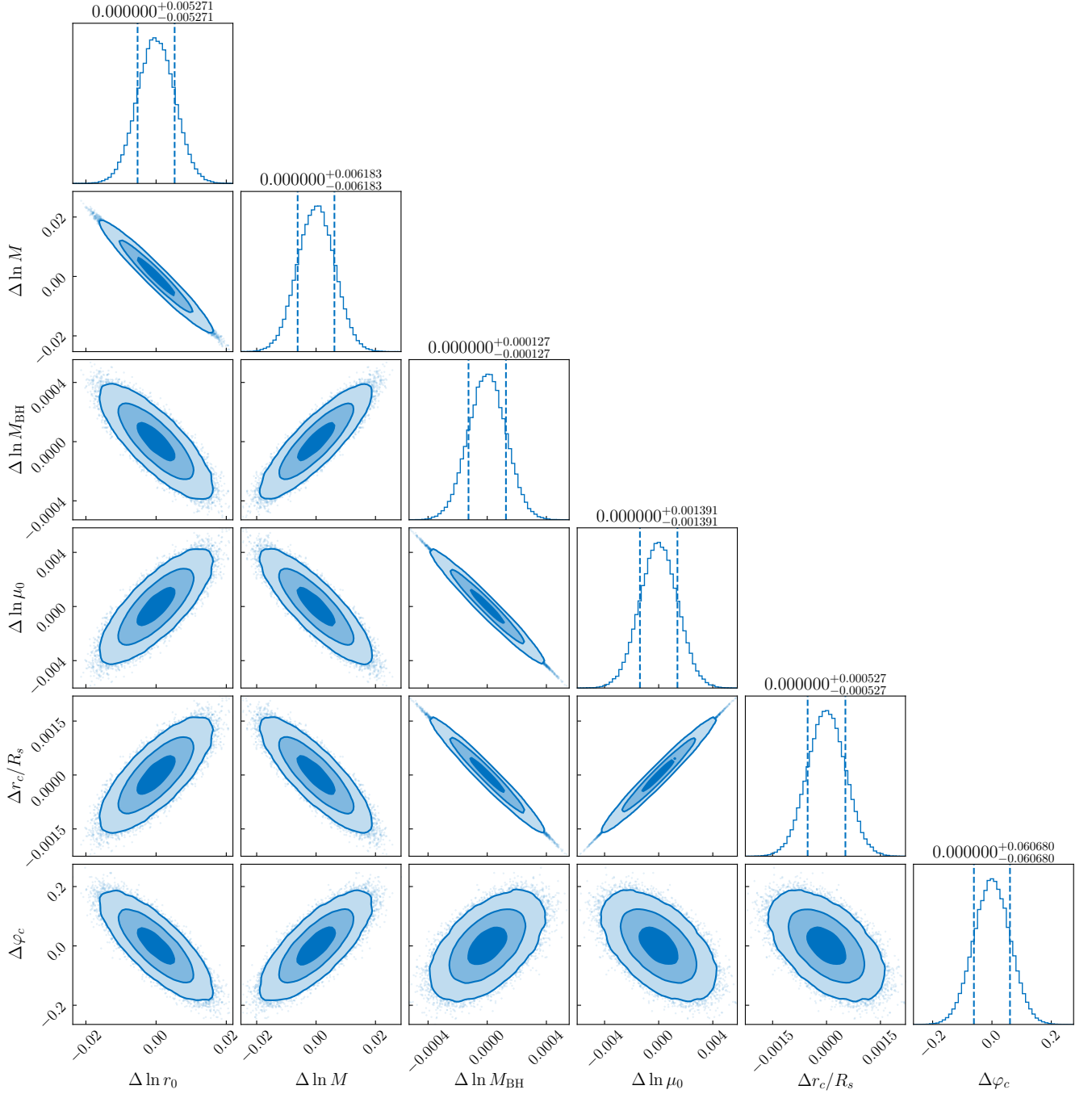


FIG. 8. Corner plot for the probability distribution of the source parameters, inferred after one-year observations with LISA. The halo parameters M/r_0 and M/r_0^2 are 10^{-1} and $10^{-6}/M_{\text{BH}}$. Vertical lines show the 1σ interval for each waveform parameter. The contours correspond to the 68%, 95%, and 99% probability confidence intervals.

precession transition happens at some critical value of p and then the prograde precessions increase as p continues to decrease.

Taking the dynamical friction, accretion, and GW reaction into account, we calculate the corresponding energy and angular momentum fluxes. We find that the effect of the GW reaction is significantly greater than those of dynamical friction and accretion when $p < 15M_{\text{BH}}$.

Furthermore, we carry out numerical calculations to study the evolution of EMRIs under the combined influences of the dynamical friction, accretion and GW reaction. We find that EMRIs immersed in DM halos evolve more slowly than those without DM. Comparing the numbers of orbital cycles with and without DM halos accumulated over one-year evolution before the merger, we find that DM halos with the compactness as small

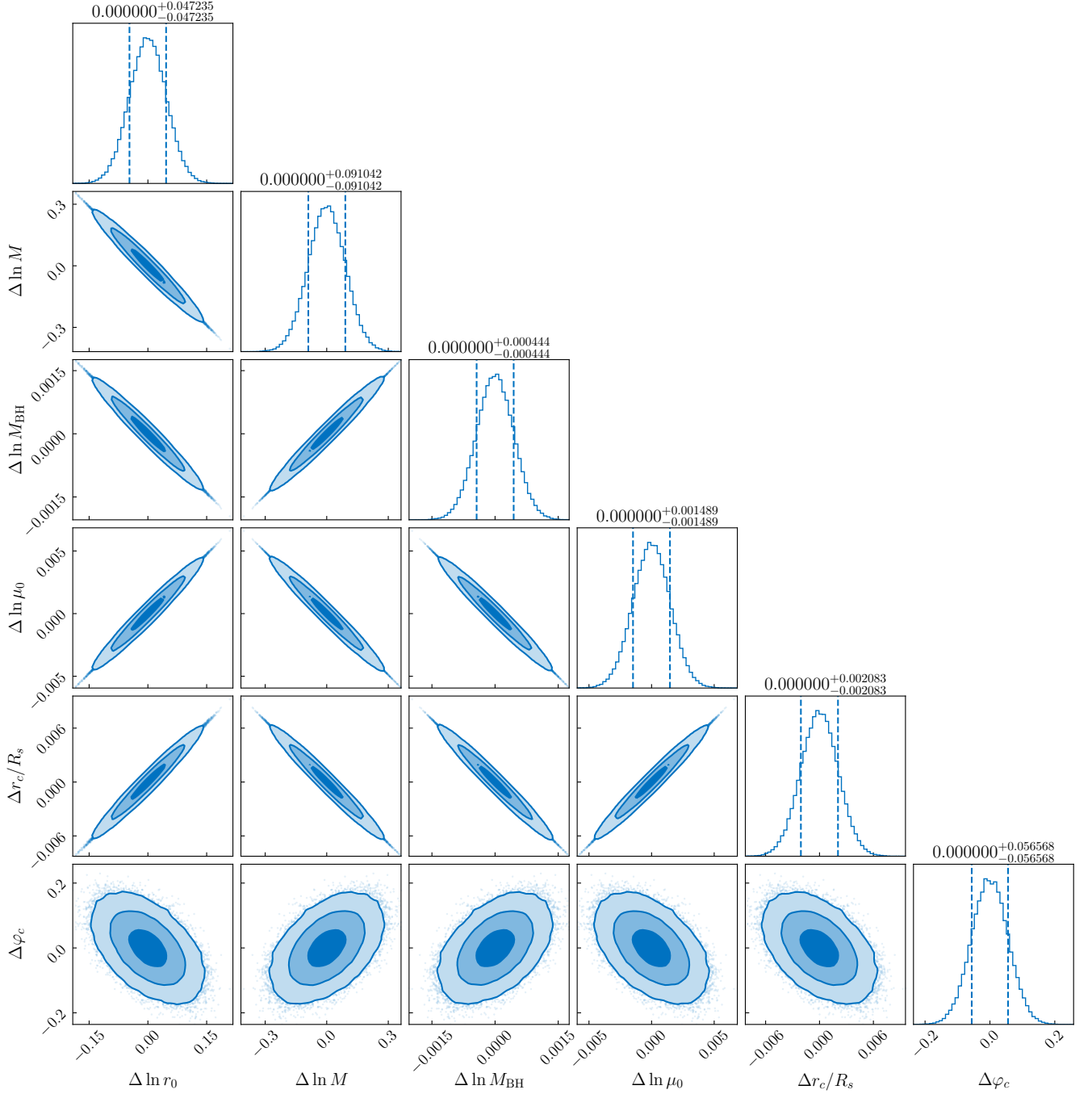


FIG. 9. Corner plot for the probability distribution of the source parameters, inferred after one-year observations with LISA. The halo parameters M/r_0 and M/r_0^2 are 10^{-2} and $10^{-6}/M_{\text{BH}}$. Vertical lines show the 1σ interval for each waveform parameter. The contours correspond to the 68%, 95%, and 99% probability confidence intervals.

as 10^{-5} can be detected. By calculating the mismatch between GW waveforms with and without DM halos, we show that we can use GWs from EMRIs within the environments of galaxies to test the existence of DM halos and detect the compactness as small as 10^{-5} . We also find that eccentric orbits can help to detect DM halos with smaller compactness. Considering the degeneracies among the source parameters, we estimated the param-

eter errors with the FIM method numerically. We find that larger values of halo compactness and density reduce the estimated errors of the parameters, and larger halo compactness helps to break the degeneracy between the parameters.

To further improve the accuracy of the GW waveform of EMRIs within DM halos, there is still a lot of work to be done. The forms of DF and accretion we used

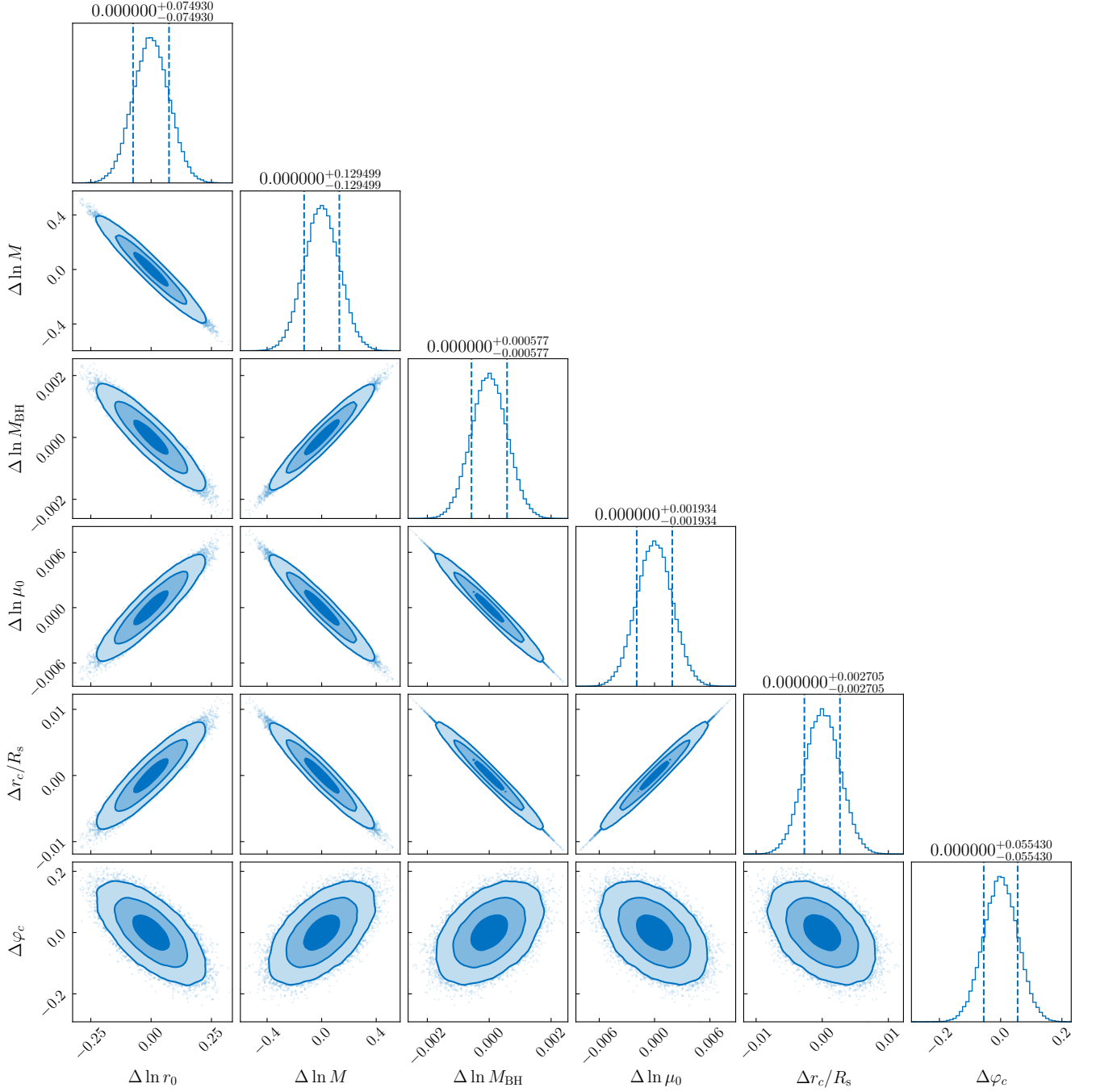


FIG. 10. Corner plot for the probability distribution of the source parameters, inferred after one-year observations with LISA. The halo parameters M/r_0 and M/r_0^2 are 10^{-2} and $10^{-7}/M_{\text{BH}}$. Vertical lines show the 1σ interval for each waveform parameter. The contours correspond to the 68%, 95%, and 99% probability confidence intervals.

are based on Newtonian estimated, and the relativistic effects of DF and accretion are not considered in this paper. Many studies have explored the relativistic effects of DF and accretion [87, 105–108]. Incorporating the relativistic effects of DF and accretion from first principles into the cases of EMRIs with DM halos deserves further attention. Compared to the perturbation black hole approach, the quadrupole formula for the energy

and angular momentum fluxes of GW used in this paper is less accurate, especially for highly eccentric orbits where higher-order multipoles are important. Currently, we are focusing on using the perturbation BH approach to study the evolution of EMRIs in DM halos, taking DF and accretion into account. We also need to consider the DM halo feedback [92, 109, 110]. To distinguish the effect of DM halos on GWs from other mediums (e.g., acce-

tion disks) or modified gravity [45, 93, 111–113], further investigation is deserved.

ACKNOWLEDGMENTS

The computing work in this paper is supported by the Public Service Platform of High Performance Computing by Network and Computing Center of HUST. This research is supported in part by the National Key Research and Development Program of China under Grant No. 2020YFC2201504.

-
- [1] B. P. Abbott *et al.* (LIGO Scientific and Virgo Collaborations), Observation of Gravitational Waves from a Binary Black Hole Merger, *Phys. Rev. Lett.* **116**, 061102 (2016).
- [2] B. P. Abbott *et al.* (LIGO Scientific and Virgo Collaborations), GW150914: The Advanced LIGO Detectors in the Era of First Discoveries, *Phys. Rev. Lett.* **116**, 131103 (2016).
- [3] B. P. Abbott *et al.* (LIGO Scientific and Virgo Collaborations), GWTC-1: A Gravitational-Wave Transient Catalog of Compact Binary Mergers Observed by LIGO and Virgo during the First and Second Observing Runs, *Phys. Rev. X* **9**, 031040 (2019).
- [4] R. Abbott *et al.* (LIGO Scientific and Virgo Collaborations), GWTC-2: Compact Binary Coalescences Observed by LIGO and Virgo During the First Half of the Third Observing Run, *Phys. Rev. X* **11**, 021053 (2021).
- [5] R. Abbott *et al.* (LIGO Scientific and Virgo Collaborations), GWTC-2.1: Deep extended catalog of compact binary coalescences observed by LIGO and Virgo during the first half of the third observing run, *Phys. Rev. D* **109**, 022001 (2024).
- [6] R. Abbott *et al.* (KAGRA, VIRGO and LIGO Scientific Collaborations), GWTC-3: Compact Binary Coalescences Observed by LIGO and Virgo during the Second Part of the Third Observing Run, *Phys. Rev. X* **13**, 041039 (2023).
- [7] K. Danzmann, LISA: An ESA cornerstone mission for a gravitational wave observatory, *Classical Quantum Gravity* **14**, 1399 (1997).
- [8] P. Amaro-Seoane *et al.* (LISA Collaboration), Laser Interferometer Space Antenna, [arXiv:1702.00786](https://arxiv.org/abs/1702.00786).
- [9] M. Colpi *et al.*, LISA Definition Study Report, [arXiv:2402.07571](https://arxiv.org/abs/2402.07571) [astro-ph.CO].
- [10] J. Luo *et al.* (TianQin Collaboration), TianQin: a space-borne gravitational wave detector, *Classical Quantum Gravity* **33**, 035010 (2016).
- [11] W.-R. Hu and Y.-L. Wu, The Taiji Program in Space for gravitational wave physics and the nature of gravity, *Natl. Sci. Rev.* **4**, 685 (2017).
- [12] Y. Gong, J. Luo, and B. Wang, Concepts and status of Chinese space gravitational wave detection projects, *Nat. Astron.* **5**, 881 (2021).
- [13] V. Baibhav *et al.*, Probing the nature of black holes: Deep in the mHz gravitational-wave sky, *Exper. Astron.* **51**, 1385 (2021).
- [14] P. A. Seoane *et al.* (LISA Collaboration), Astrophysics with the Laser Interferometer Space Antenna, *Living Rev. Relativity* **26**, 2 (2023).
- [15] K. G. Arun *et al.* (LISA Collaboration), New horizons for fundamental physics with LISA, *Living Rev. Relativity* **25**, 4 (2022).
- [16] N. Karnesis *et al.*, The Laser Interferometer Space Antenna mission in Greece White Paper, [arXiv:2209.04358](https://arxiv.org/abs/2209.04358).
- [17] S. Babak, J. Gair, A. Sesana, E. Barausse, C. F. Sopuerta, C. P. L. Berry, E. Berti, P. Amaro-Seoane, A. Petiteau, and A. Klein, Science with the space-based interferometer LISA. V: Extreme mass-ratio inspirals, *Phys. Rev. D* **95**, 103012 (2017).
- [18] P. Amaro-Seoane, J. R. Gair, M. Freitag, M. Coleman Miller, I. Mandel, C. J. Cutler, and S. Babak, Astrophysics, detection and science applications of intermediate- and extreme mass-ratio inspirals, *Classical Quantum Gravity* **24**, R113 (2007).
- [19] C. P. L. Berry, S. A. Hughes, C. F. Sopuerta, A. J. K. Chua, A. Heffernan, K. Holley-Bockelmann, D. P. Mihaylov, M. C. Miller, and A. Sesana, The unique potential of extreme mass-ratio inspirals for gravitational-wave astronomy, [arXiv:1903.03686](https://arxiv.org/abs/1903.03686).
- [20] P. A. Seoane *et al.*, The effect of mission duration on LISA science objectives, *Gen. Relativ. Gravit.* **54**, 3 (2022).
- [21] D. Laghi, N. Tamanini, W. Del Pozzo, A. Sesana, J. Gair, S. Babak, and D. Izquierdo-Villalba, Gravitational-wave cosmology with extreme mass-ratio inspirals, *Mon. Not. R. Astron. Soc.* **508**, 4512 (2021).
- [22] S. McGee, A. Sesana, and A. Vecchio, Linking gravitational waves and X-ray phenomena with joint LISA and Athena observations, *Nat. Astron.* **4**, 26 (2020).
- [23] S. van den Bergh, The Early history of dark matter, *Publ. Astron. Soc. Pac.* **111**, 657 (1999).
- [24] V. C. Rubin and W. K. Ford, Jr., Rotation of the Andromeda Nebula from a Spectroscopic Survey of Emission Regions, *Astrophys. J.* **159**, 379 (1970).
- [25] V. C. Rubin, N. Thonnard, and W. K. Ford, Jr., Rotational properties of 21 SC galaxies with a large range of luminosities and radii, from NGC 4605 /R = 4kpc/ to UGC 2885 /R = 122 kpc/, *Astrophys. J.* **238**, 471 (1980).
- [26] K. G. Begeman, A. H. Broeils, and R. H. Sanders, Extended rotation curves of spiral galaxies: Dark haloes and modified dynamics, *Mon. Not. R. Astron. Soc.* **249**, 523 (1991).
- [27] M. Persic, P. Salucci, and F. Stel, The Universal rotation curve of spiral galaxies: 1. The Dark matter connection, *Mon. Not. R. Astron. Soc.* **281**, 27 (1996).
- [28] E. Corbelli and P. Salucci, The Extended Rotation Curve and the Dark Matter Halo of M33, *Mon. Not. R. Astron. Soc.* **311**, 441 (2000).

- [29] L. A. Moustakas *et al.*, Strong gravitational lensing probes of the particle nature of dark matter, [arXiv:0902.3219](#).
- [30] R. Massey, T. Kitching, and J. Richard, The dark matter of gravitational lensing, *Rept. Prog. Phys.* **73**, 086901 (2010).
- [31] J. Ellis and K. A. Olive, Supersymmetric Dark Matter Candidates, [arXiv:1001.3651](#).
- [32] A. Challinor, CMB anisotropy science: a review, *IAU Symp.* **288**, 42 (2013).
- [33] L. Sadeghian, F. Ferrer, and C. M. Will, Dark matter distributions around massive black holes: A general relativistic analysis, *Phys. Rev. D* **88**, 063522 (2013).
- [34] J. F. Navarro, C. S. Frenk, and S. D. M. White, A Universal density profile from hierarchical clustering, *Astrophys. J.* **490**, 493 (1997).
- [35] P. Gondolo and J. Silk, Dark matter annihilation at the galactic center, *Phys. Rev. Lett.* **83**, 1719 (1999).
- [36] L. Hernquist, An Analytical Model for Spherical Galaxies and Bulges, *Astrophys. J.* **356**, 359 (1990).
- [37] N. Yunes, B. Kocsis, A. Loeb, and Z. Haiman, Imprint of Accretion Disk-Induced Migration on Gravitational Waves from Extreme Mass Ratio Inspirals, *Phys. Rev. Lett.* **107**, 171103 (2011).
- [38] B. Kocsis, N. Yunes, and A. Loeb, Observable Signatures of EMRI Black Hole Binaries Embedded in Thin Accretion Disks, *Phys. Rev. D* **84**, 024032 (2011).
- [39] K. Eda, Y. Itoh, S. Kuroyanagi, and J. Silk, New Probe of Dark-Matter Properties: Gravitational Waves from an Intermediate-Mass Black Hole Embedded in a Dark-Matter Minispikes, *Phys. Rev. Lett.* **110**, 221101 (2013).
- [40] C. F. B. Macedo, P. Pani, V. Cardoso, and L. C. B. Crispino, Into the lair: gravitational-wave signatures of dark matter, *Astrophys. J.* **774**, 48 (2013).
- [41] K. Eda, Y. Itoh, S. Kuroyanagi, and J. Silk, Gravitational waves as a probe of dark matter minispikes, *Phys. Rev. D* **91**, 044045 (2015).
- [42] E. Barausse, V. Cardoso, and P. Pani, Can environmental effects spoil precision gravitational-wave astrophysics?, *Phys. Rev. D* **89**, 104059 (2014).
- [43] L. Barack *et al.*, Black holes, gravitational waves and fundamental physics: a roadmap, *Classical Quantum Gravity* **36**, 143001 (2019).
- [44] O. A. Hannuksela, K. W. K. Wong, R. Brito, E. Berti, and T. G. F. Li, Probing the existence of ultralight bosons with a single gravitational-wave measurement, *Nat. Astron.* **3**, 447 (2019).
- [45] V. Cardoso and A. Maselli, Constraints on the astrophysical environment of binaries with gravitational-wave observations, *Astron. Astrophys.* **644**, A147 (2020).
- [46] X.-J. Yue and Z. Cao, Dark matter minispikes: A significant enhancement of eccentricity for intermediate-mass-ratio inspirals, *Phys. Rev. D* **100**, 043013 (2019).
- [47] L. Annulli, V. Cardoso, and R. Vicente, Stirred and shaken: Dynamical behavior of boson stars and dark matter cores, *Phys. Lett. B* **811**, 135944 (2020).
- [48] A. Derdzinski, D. D’Orazio, P. Duffell, Z. Haiman, and A. MacFadyen, Evolution of gas disc-embedded intermediate mass ratio inspirals in the *LISA* band, *Mon. Not. R. Astron. Soc.* **501**, 3540 (2021).
- [49] L. Zwick, P. R. Capelo, and L. Mayer, Priorities in gravitational waveforms for future space-borne detectors: vacuum accuracy or environment?, *Mon. Not. R. Astron. Soc.* **521**, 4645 (2023).
- [50] N. Dai, Y. Gong, T. Jiang, and D. Liang, Intermediate mass-ratio inspirals with dark matter minispikes, *Phys. Rev. D* **106**, 064003 (2022).
- [51] A. Coogan, G. Bertone, D. Gaggero, B. J. Kavanagh, and D. A. Nichols, Measuring the dark matter environments of black hole binaries with gravitational waves, *Phys. Rev. D* **105**, 043009 (2022).
- [52] H. Kim, A. Lenoci, I. Stomberg, and X. Xue, Adiabatically compressed wave dark matter halo and intermediate-mass-ratio inspirals, *Phys. Rev. D* **107**, 083005 (2023).
- [53] V. Cardoso, K. Destounis, F. Duque, R. P. Macedo, and A. Maselli, Black holes in galaxies: Environmental impact on gravitational-wave generation and propagation, *Phys. Rev. D* **105**, L061501 (2022).
- [54] A. Einstein, On a stationary system with spherical symmetry consisting of many gravitating masses, *Annals Math.* **40**, 922 (1939).
- [55] A. Geralico, F. Pompei, and R. Ruffini, On Einstein clusters, *Int. J. Mod. Phys. Conf. Ser.* **12**, 146 (2012).
- [56] R. A. Konoplya and A. Zhidenko, Solutions of the Einstein Equations for a Black Hole Surrounded by a Galactic Halo, *Astrophys. J.* **933**, 166 (2022).
- [57] K. Jusufi, Black holes surrounded by Einstein clusters as models of dark matter fluid, *Eur. Phys. J. C* **83**, 103 (2023).
- [58] Z. Shen, A. Wang, Y. Gong, and S. Yin, Analytical models of supermassive black holes in galaxies surrounded by dark matter halos, *Phys. Lett. B* **855**, 138797 (2024).
- [59] J. Liu, S. Chen, and J. Jing, Tidal effects of a dark matter halo around a galactic black hole*, *Chin. Phys. C* **46**, 105104 (2022).
- [60] K. Destounis, A. Kulathingal, K. D. Kokkotas, and G. O. Papadopoulos, Gravitational-wave imprints of compact and galactic-scale environments in extreme-mass-ratio binaries, *Phys. Rev. D* **107**, 084027 (2023).
- [61] V. Cardoso, K. Destounis, F. Duque, R. Panosso Macedo, and A. Maselli, Gravitational Waves from Extreme-Mass-Ratio Systems in Astrophysical Environments, *Phys. Rev. Lett.* **129**, 241103 (2022).
- [62] Y. Kozai, Secular perturbations of asteroids with high inclination and eccentricity, *Astron. J.* **67**, 591 (1962).
- [63] D. C. Heggie, Binary evolution in stellar dynamics, *Mon. Not. R. Astron. Soc.* **173**, 729 (1975).
- [64] F. Antonini, S. Toonen, and A. S. Hamers, Binary black hole mergers from field triples: properties, rates and the impact of stellar evolution, *Astrophys. J.* **841**, 77 (2017).
- [65] B.-M. Hoang, S. Naoz, B. Kocsis, W. Farr, and J. McIver, Detecting Supermassive Black Hole-induced Binary Eccentricity Oscillations with *LISA*, *Astrophys. J. Lett.* **875**, L31 (2019).
- [66] L. Wen, On the eccentricity distribution of coalescing black hole binaries driven by the Kozai mechanism in globular clusters, *Astrophys. J.* **598**, 419 (2003).
- [67] M. C. Miller and D. P. Hamilton, Four-body effects in globular cluster black hole coalescence, *Astrophys. J.* **576**, 894 (2002).
- [68] C. Cutler, D. Kennefick, and E. Poisson, Gravitational radiation reaction for bound motion around a Schwarzschild black hole, *Phys. Rev. D* **50**, 3816 (1994).
- [69] J. R. Gair and K. Glampedakis, Improved approximate inspirals of test-bodies into Kerr black holes, *Phys. Rev.*

- D 73**, 064037 (2006).
- [70] V. Cardoso, C. F. B. Macedo, and R. Vicente, Eccentricity evolution of compact binaries and applications to gravitational-wave physics, *Phys. Rev. D* **103**, 023015 (2021).
- [71] T. Jiang, N. Dai, Y. Gong, D. Liang, and C. Zhang, Constraint on Brans-Dicke theory from intermediate/extreme mass ratio inspirals, *J. Cosmol. Astropart. Phys.* **12** (2022) 023.
- [72] S. Barsanti, N. Franchini, L. Gualtieri, A. Maselli, and T. P. Sotiriou, Extreme mass-ratio inspirals as probes of scalar fields: Eccentric equatorial orbits around Kerr black holes, *Phys. Rev. D* **106**, 044029 (2022).
- [73] T. Yang, R.-G. Cai, Z. Cao, and H. M. Lee, Eccentricity of Long Inspiring Compact Binaries Sheds Light on Dark Sirens, *Phys. Rev. Lett.* **129**, 191102 (2022).
- [74] S. Chandrasekhar, Dynamical Friction. I. General Considerations: the Coefficient of Dynamical Friction, *Astrophys. J.* **97**, 255 (1943).
- [75] H. Bondi and F. Hoyle, On the mechanism of accretion by stars, *Mon. Not. R. Astron. Soc.* **104**, 273 (1944).
- [76] R. G. Edgar, A Review of Bondi-Hoyle-Lyttleton accretion, *New Astron. Rev.* **48**, 843 (2004).
- [77] J. R. Gair, D. J. Kennefick, and S. L. Larson, Semi-relativistic approximation to gravitational radiation from encounters with black holes, *Phys. Rev. D* **72**, 084009 (2005), [Erratum: *Phys.Rev.D* 74, 109901 (2006)].
- [78] S. Babak, H. Fang, J. R. Gair, K. Glampedakis, and S. A. Hughes, 'Kludge' gravitational waveforms for a test-body orbiting a Kerr black hole, *Phys. Rev. D* **75**, 024005 (2007), [Erratum: *Phys.Rev.D* 77, 04990 (2008)].
- [79] J. E. Taylor and J. Silk, The Clumpiness of cold dark matter: Implications for the annihilation signal, *Mon. Not. R. Astron. Soc.* **339**, 505 (2003).
- [80] A. Burkert, The Structure of dark matter halos in dwarf galaxies, *Astrophys. J. Lett.* **447**, L25 (1995).
- [81] E. Figueiredo, A. Maselli, and V. Cardoso, Black holes surrounded by generic dark matter profiles: Appearance and gravitational-wave emission, *Phys. Rev. D* **107**, 104033 (2023).
- [82] N. Speeney, E. Berti, V. Cardoso, and A. Maselli, Black holes surrounded by generic matter distributions: Polar perturbations and energy flux, *Phys. Rev. D* **109**, 084068 (2024).
- [83] M. Pierre, J. M. Siegal-Gaskins, and P. Scott, Sensitivity of CTA to dark matter signals from the Galactic Center, *J. Cosmol. Astropart. Phys.* **06** (2014) 024, [Erratum: *JCAP* 10, E01 (2014)].
- [84] F. Iocco, M. Pato, and G. Bertone, Evidence for dark matter in the inner Milky Way, *Nature Phys.* **11**, 245 (2015).
- [85] T. Igata and Y. Takamori, Periapsis shifts in dark matter distribution with a dense core, *Phys. Rev. D* **105**, 124029 (2022).
- [86] T. Igata, T. Harada, H. Saida, and Y. Takamori, Periapsis shifts in dark matter distribution around a black hole, *Int. J. Mod. Phys. D* **32**, 2350105 (2023).
- [87] S. A. Hughes, Bound orbits of a slowly evolving black hole, *Phys. Rev. D* **100**, 064001 (2019).
- [88] B. Blachier, A. Barrau, K. Martineau, and C. Renevey, Competitive effects between gravitational radiation and mass variation for two-body systems in circular orbits, *Gen. Relativ. Gravit.* **56**, 20 (2024).
- [89] P. C. Peters and J. Mathews, Gravitational radiation from point masses in a Keplerian orbit, *Phys. Rev.* **131**, 435 (1963).
- [90] P. C. Peters, Gravitational Radiation and the Motion of Two Point Masses, *Phys. Rev.* **136**, B1224 (1964).
- [91] E. Berti, A. Buonanno, and C. M. Will, Estimating spinning binary parameters and testing alternative theories of gravity with LISA, *Phys. Rev. D* **71**, 084025 (2005).
- [92] B. J. Kavanagh, D. A. Nichols, G. Bertone, and D. Gaggero, Detecting dark matter around black holes with gravitational waves: Effects of dark-matter dynamics on the gravitational waveform, *Phys. Rev. D* **102**, 083006 (2020).
- [93] A. Maselli, N. Franchini, L. Gualtieri, and T. P. Sotiriou, Detecting scalar fields with Extreme Mass Ratio Inspirals, *Phys. Rev. Lett.* **125**, 141101 (2020).
- [94] T. Robson, N. J. Cornish, and C. Liu, The construction and use of LISA sensitivity curves, *Classical Quantum Gravity* **36**, 105011 (2019).
- [95] E. E. Flanagan and S. A. Hughes, Measuring gravitational waves from binary black hole coalescences: 2. The Waves' information and its extraction, with and without templates, *Phys. Rev. D* **57**, 4566 (1998).
- [96] L. Lindblom, B. J. Owen, and D. A. Brown, Model Waveform Accuracy Standards for Gravitational Wave Data Analysis, *Phys. Rev. D* **78**, 124020 (2008).
- [97] C. Cutler and E. E. Flanagan, Gravitational waves from merging compact binaries: How accurately can one extract the binary's parameters from the inspiral wave form?, *Phys. Rev. D* **49**, 2658 (1994).
- [98] E. Poisson and C. M. Will, Gravitational waves from inspiraling compact binaries: Parameter estimation using second post-Newtonian wave forms, *Phys. Rev. D* **52**, 848 (1995).
- [99] C. Cutler, Angular resolution of the LISA gravitational wave detector, *Phys. Rev. D* **57**, 7089 (1998).
- [100] C. M. Will, Testing scalar - tensor gravity with gravitational wave observations of inspiraling compact binaries, *Phys. Rev. D* **50**, 6058 (1994).
- [101] A. Maselli, N. Franchini, L. Gualtieri, T. P. Sotiriou, S. Barsanti, and P. Pani, Detecting fundamental fields with LISA observations of gravitational waves from extreme mass-ratio inspirals, *Nat. Astron.* **6**, 464 (2022).
- [102] C. Zhang, G. Fu, and N. Dai, Detecting dark matter halos with extreme mass-ratio inspirals, *J. Cosmol. Astropart. Phys.* **04** (2024) 088.
- [103] E. Berti *et al.*, Testing General Relativity with Present and Future Astrophysical Observations, *Classical Quantum Gravity* **32**, 243001 (2015).
- [104] K. Yagi and T. Tanaka, Constraining alternative theories of gravity by gravitational waves from precessing eccentric compact binaries with LISA, *Phys. Rev. D* **81**, 064008 (2010), [Erratum: *Phys.Rev.D* 81, 109902 (2010)].
- [105] N. Speeney, A. Antonelli, V. Baibhav, and E. Berti, Impact of relativistic corrections on the detectability of dark-matter spikes with gravitational waves, *Phys. Rev. D* **106**, 044027 (2022), arXiv:2204.12508 [gr-qc].
- [106] R. Vicente and V. Cardoso, Dynamical friction of black holes in ultralight dark matter, *Phys. Rev. D* **105**, 083008 (2022), arXiv:2201.08854 [gr-qc].
- [107] D. Traykova, R. Vicente, K. Clough, T. Helfer, E. Berti, P. G. Ferreira, and L. Hui, Relativistic drag forces on

- black holes from scalar dark matter clouds of all sizes, *Phys. Rev. D* **108**, L121502 (2023), [arXiv:2305.10492 \[gr-qc\]](#).
- [108] P. Mach and A. Odrzywo, Accretion of Dark Matter onto a Moving Schwarzschild Black Hole: An Exact Solution, *Phys. Rev. Lett.* **126**, 101104 (2021), [arXiv:2103.03595 \[gr-qc\]](#).
- [109] N. Becker, L. Sagunski, L. Prinz, and S. Rastgoo, Circularization versus eccentricification in intermediate mass ratio inspirals inside dark matter spikes, *Phys. Rev. D* **105**, 063029 (2022).
- [110] T. K. Karydas, B. J. Kavanagh, and G. Bertone, Sharpening the dark matter signature in gravitational waveforms I: Accretion and eccentricity evolution, [arXiv:2402.13053](#).
- [111] N. Becker and L. Sagunski, Comparing accretion disks and dark matter spikes in intermediate mass ratio inspirals, *Phys. Rev. D* **107**, 083003 (2023).
- [112] C. Zhang and Y. Gong, Detecting electric charge with extreme mass ratio inspirals, *Phys. Rev. D* **105**, 124046 (2022).
- [113] V. Cardoso, G. Castro, and A. Maselli, Gravitational waves in massive gravity theories: waveforms, fluxes and constraints from extreme-mass-ratio mergers, *Phys. Rev. Lett.* **121**, 251103 (2018).